PHYLLOSILICATE EMISSION FROM PROTOPLANETARY DISKS

by

Melissa A. Morris

A Thesis Presented in Partial Fulfillment
of the Requirements for the Degree
Master of Science

ARIZONA STATE UNIVERSITY

May 2007

PHYLLOSILICATE EMISSION FROM PROTOPLANETARY DISKS

by

Melissa A. Morris

has been approved

November 2006

APPROVED:

_____, Chair

_____

_____

Supervisory Committee

ACCEPTED:

_____

Department Chair

_____

Dean, Division of Graduate Studies

ABSTRACT

Phyllosilicates are commonly found in meteorites. A product of aqueous alteration, phyllosilicates have unique emission features in the mid-infrared. In order to determine if these features can be detected in extrasolar protoplanetary disks with instruments such as the Spitzer Space Telescope, disk emission was modeled using simple radiative transfer. In so doing, it was found that the most prominent phyllosilicate features can be detected. Comparisons of the disk emission model with and without the inclusion of 3% phyllosilicates in the dust mixture are presented. The zodiacal dust in our Solar System has been modeled by including 20% montmorillonite, a phyllosilicate. Detection of phyllosilicates in extrasolar protoplanetary disks, indicates the presence of liquid water, and would demonstrate a similarity of those disks to our Solar System. Non-detection would place a meaningful upper limit on the abundance of phyllosilicates and would imply that those systems are fundamentally different than our own.

For my mom...I've missed her each and every day of this journey.

ACKNOWLEDGMENTS

I would like to thank all those senior graduate students and post docs who have helped me with my many Unix, LaTex, and IDL questions. Matt Beasley certainly made the transition to Mac that much smoother. Both Nic Ouellette and Joe Foy have answered a variety of questions over the years. I would certainly have had a much harder time learning IDL if it weren't for the patience and wisdom of Kevin Healy. Thanks to Tom Sharp and Phil Christensen for the information and advice on minerals, in general, and phyllosilicates, in particular. Thanks to Peter Buseck for the conversation on phyllosilicates found in meteorites and for pointing me in the direction of Laurence Garvie, who graciously provided me with a sample of cronstedtite. Many thanks go to Joe Michalski for the great discussions about minerals, putting me in contact with Tim Glotch, providing clay samples to Tim for use in his measurements, and for putting up with my multitude of questions. I would like to extend my utmost appreciation to Tim Glotch for his meticulous work in measuring the optical constants of the samples provided. This work certainly would not have come about without his efforts.

Jeff Hester deserves my heart-felt thanks for the many questions he has enthusiastically answered over the years, along with his sound advice on many fronts. He showed infinite patience even when he was busy or times were rough. Special thanks go to Jason Cook, who not only has answered more questions than I care to remember and been an excellent office-mate, but has also given me the gift of some of the best discussions I can remember about science and our mutual research interests...not to mention allowing me the opportunity to see the inside of a telescope control room again.

I would like to acknowledge the support, both financial and otherwise, of my advisor, Steve Desch, without whom this research would not have been possible. I would also like to

thank my good friend, Jana, for her encouragement and unfailing confidence in my abilities. I can't begin to thank my boyfriend, Gary, enough for reminding me that there is much more to life than work, for showing me all the beauty and variety the area has to offer, for being such a calming influence (who somehow, miraculously, takes all the stress away), and for helping to create so many wonderful memories...may there be many more. Last, but not least, I would like to express my appreciation for the patience of my son, Chase, who has given up many home-cooked meals and good conversations for the sake of this work.

TABLE OF CONTENTS

Page

Page

Page

LIST OF TABLES

LIST OF FIGURES

Figure Page

CHAPTER 1

INTRODUCTION

It is now generally believed that the majority of Earth's water was delivered by planetesimals from the outer asteroid belt (Morbidelli et al. 2000; Raymond et al. 2004). The deuterium to hydrogen ratio (D/H) in VSMOW (Vienna mean standard ocean water) is consistent with that of carbonaceous chondrites, both having D/H ratios of 150 x 10^{-6} (Drake & Righter 2002). Carbonaceous chondrites, believed to have formed in the outer asteroid belt, contain $\sim$ 10 wt% water, whereas ordinary and enstatite chondrites, which formed in the inner belt, contain $\sim$ 0.5-0.1 wt% water (Morbidelli et al. 2000). It is expected that even less water would have been incorporated into planetesimals in the vicinity of Earth's orbit, possibly explaining why the mass fraction of water on Earth is only $\sim 10^{-4}$ (Morbidelli et al. 2000). In the past, it was suggested that most of Earth's water was delivered by comets. However, both Ar/H_2O and D/H data suggest otherwise (Drake & Righter 2002). In fact, D/H in comets is twice that for Earth (Morbidelli 2000). During its formation, Earth received no more than 50% of its water from comets (Drake & Righter 2002), with comets accounting for, at most, 10% of the Earth's present water budget (Morbidelli et al. 2000). Both Drake & Righter (2002) and Morbidelli et al. (2000) strongly argue that the Earth accreted "wet", with asteroids and planetesimals from the outer belt as the main source of the water.

The water contained in carbonaceous chondrites is mainly in the form of hydrous minerals known as phyllosilicates. Phyllosilicates are the major mineral product of aqueous alteration of silicate rock. Aqueous alteration on the parent body is believed to account for the majority of the phyllosilicates found in meteorites. These parent bodies not only produced the meteorites, but have shed dust due to collisions. The zodiacal dust in our Solar System is thought to originate from such collisions and the sublimation of comets. In their model of the zodiacal dust, it was necessary for Reach et al. (2003) to include 20% mont-

morillonite ($[Na,Ca]_{0.33}[Al,Mg]_2Si_4O_{10}[OH]_2 \cdot n[H_2O]$), a phyllosilicate, in order to match the observed spectra. If extrasolar protoplanetary disks are similar to our Solar System, in that they contain planetesimals which have undergone aqueous alteration, those planetesimals should contain significant amounts of phyllosilicates. Collisions of these hydrated parent bodies should produce an "extrasolar zodiacal dust" containing phyllosilicates.

The focus of this investigation is to determine whether phyllosilicates can be detected in extrasolar protoplanetary disks by instruments such as the Spitzer Space Telescope. Phyllosilicates have characteristic emission features in the mid-infrared which are potentially observable in protoplanetary and/or debris disks. In order to proceed with the investigation, it is necessary to have a general understanding of the phyllosilicate minerals themselves, appropriate disk environments, and the instruments which may be used to detect the emission.

1. Phyllosilicates

Phyllosilicates are hydrous sheet silicates, sometimes referred to as layer silicates. The term phyllosilicates derives from the Greek "phyllon", meaning leaf, alluding to the flaky or platy habit of the minerals (think phyllo dough) (Nesse 2000).

Sheet silicates exhibit two different types: octahedral (O) sheets, made up of two planes of anionic groups, and tetrahedral (T) sheets, consisting of tetrahedrally coordinated cations. Octahedral sheets may be dioctahedral or trioctahedral, depending on whether the octahedral sites formed between the anionic groups are occupied by divalent (e.g. Fe^{2+}, Mg^{2+}) or trivalent (e.g. Al^{3+}) cations. O and T sheets are joined together to form layers. These layers are then stacked on top of each other to form the overall structure of the mineral. The weak bonding between layers produces the single perfect cleavage characteristic

of the phyllosilicates (Nesse 2000).

Phyllosilicates are the major mineral product of aqueous alteration of silicate rock. For example, serpentine, a phyllosilicate, is commonly formed by hydrothermal alteration of mafic or ultramafic rock containing olivine and pyroxene (Nesse 2000). The interaction of silicic rock and water at low temperature produces clay minerals, such as saponite ($[Ca/2,Na]_{0.33}[Mg,Fe^{2+}]_3[Si,Al]_4O_{10}[OH]_2 \cdot 4H_2O$) and montmorillonite (Nesse 2000; Grim 1968). [Clay minerals are defined as fine-grained (< 0.002 mm) sheet silicates]. The clay minerals that form depend on the parent rock, the temperature, the amount and chemistry of the water, and time (Velde 1995; Weaver 1989). For example, montmorillonite forms in an alkaline environment, whereas kaolinite ($Al_2Si_2O_5[OH]_4$) forms in an acidic environment (Grim 1968).

Earth and the other terrestrial planets ultimately formed from materials which condensed out of the solar nebula. Samples of this material are preserved in the class of meteorites known as *chondrites*, which have ages of approximately 4.55 Gyr (Carr 1996; Wadhwa & Russell 2000). Chondrites are characterized by the presence of spherical droplets called *chondrules* (Carr 1996). Most chondrules range in size from 0.01-0.1 mm in diameter, and are commonly believed to have been formed by high-energy events, such as nebular shocks (Wadhwa & Russell 2000; Desch & Connolly 2002; Desch et al. 2005), which involved melting of pre-existing solids in the solar nebula (Carr 1996; Wadhwa & Russell 2000). Over 70% of meteorite falls are ordinary chondrites, consisting mainly of high-temperature ($T > 400^\circ$ C) minerals, but approximately 5% of meteorites are carbonaceous chondrites. The chondrules in carbonaceous chondrites are embedded in a fine-grained matrix of mostly hydrated, low-temperature minerals, such as phyllosilicates (Carr 1996). In the subclass of CI charbonaceous chondrites, anywhere from 40% to over 90% of the volume is made

up of fine-grained phyllosilicates and associated phases (Tomeoka & Buseck 1990; Buseck & Hua 1993; Rubin 1997). Phyllosilicates are also often found in fine-grained rims around chondrules (Ciesla et al. 2003 and references therein).

Virtually all carbonaceous chondrites contain phyllosilicates, with the different amounts indicating varying degrees of aqueous alteration. The subclasses which have experienced the most alteration are the CI, CM, and CR chondrites (Buseck & Hua 1993; Rubin 1997), which are significantly more altered than the CO and CV chondrites. The most common phyllosilicates found in meteorites are overwhelmingly saponite and serpentine ($[Mg,Fe]_3Si_2O_5[OH]_4$), with montmorillonite identified in a small number of samples. The phyllosilicates found in the matrix are almost always Fe-rich (Tomeoka & Buseck 1985; Buseck & Hua 1993), as opposed to the phyllosilicates found in the accretionary rims of chondrules, which are usually Mg-rich (Lauretta et al. 2000). This possibly indicates a different method and/or time of formation.

In their review of 1993, Buseck and Hua found that the occurrence of saponite and serpentine was roughly equal in the matrix of the carbonaceous chondrites. The phyllosilicate found in the matrix of the CI and the CV chondrites was saponite, serpentine in the CMs and COs, and both saponite and serpentine were found within the matrix of the CR chondrites. (Some serpentine was found within the chondrules of the CV chondrites). Saponite is also found in ordinary chondrites and interplanetary dust particles (IDPs) (Keller & Zolensky 1991). In the four phyllosilicate-rich micrometeorites investigated by Noguchi et al. (2002), three were found to be saponite-rich and one was serpentine-rich. They also determined that the two phyllosilicates did not coexist in any of the four micrometeorites studied (Noguchi et al. 2002). Whether saponite or serpentine is found probably reflects the temperature during alteration (Keller & Buseck 1990), and, to a lesser extent,

Table 1. Phyllosilicates found in chondrites

Saponite	Serpentine	Montmorillonite	Cronstedtite
CI	CM	CI	CM
CV	CO		
CR	CR		
ord. chond.			
IDPs			

the parent mineralogy (Krishna Swamy 2005), with saponite usually forming from enstatite ($MgSiO_3$) and serpentine from olivine (an exception is the saponite in the CV chondrite Mokoia, believed to have formed from Fe-rich olivine (Tomeoka & Buseck 1985)). For example, although serpentine is the most common alteration product of terrestrial olivine, saponite will form from olivine in oxidizing conditions with temperatures less than 140° C, where serpentine will NOT (Tomeoka & Buseck 1990).

Montmorillonite has been identified in the matrix of some CI chondrites and in the phyllosilicate rims of chondrules (Buseck & Hua 1993). Cronstedtite ($Fe^{2+}_2Fe^{3+}[Si, Fe^{3+}]O_5[OH]_4$), a Fe-rich phyllosilicate (Lauretta 2000; Buseck & Hua 1993) rarely found terrestrially, makes up the bulk of the matrix of CM chondrites, along with intergrowths of serpentine (Buseck & Hua 1993). The phyllosilicates found in the matrix of carbonaceous chondrites is summarized in Table 1.

The type of phyllosilicate ultimately produced not only depends on such things as parent rock and temperature, but may depend on the time and/or place of formation. Some authors favor a parent body origin for the phyllosilicates found in meteorites (Armstrong et al. 1982; Tomeoka & Buseck 1985; Buseck & Hua 1993; Kerridge et al. 1994; Browning et al. 1994; Krot et al. 1995; Scott & Krot 2005), while others favor a nebular formation for at least some (Hashimoto & Grossman 1987; MacPherson et al. 1982, 1983; Clayton 1997;

Ciesla et al. 2003; Nuth et al. 2005). Yet others believe that the phyllosilicates found in the matrix of meteorites (or certain classes of meteorites) lend themselves to a parent body origin, whereas those found in accretionary rims are more likely to have formed in the solar nebula prior to incorporation into the parent body (Tomeoka 1993; Schirmeyer et al. 1997; Bischoff 1998). At any rate, all the phyllosilicates found in meteorites are the products of aqueous alteration, which makes them an excellent tracer of water. Whether the alteration occurred in the nebula or on the parent bodies of meteorites, it seems that the alteration and resulting phyllosilicates were ubiquitous during the early stages of the formation of the Solar System.

2. Disk Environments

2.1. *Nebular versus Parent Body Alteration*

The meteoritic evidence certainly indicates the presence of phyllosilicates early in the Solar System, however it is not clear just how early. Better understanding of their origin is needed in order to determine if they were present while there was still a disk. There is an ongoing controversy as to whether the aqueous alteration which produced the phyllosilicates found in meteorites occurred in the solar nebula or on parent bodies. If, in fact, all aqueous alteration occurs only on parent bodies, the existence of planetesimals would be required in order for phyllosilicates to be detectable in a disk. This would necessitate the passage of enough time for planetesimals to form (up to a few Myr) before detection would be possible. On the other hand, if phyllosilicates can form in the gas phase, detection may be possible in very young disks.

CM Chondrites. Most authors agree that the majority of the phyllosilicates in CM chondrites and, quite possibly, *all* of the phyllosilicates in CI chondrites are the result of parent body processes (Bischoff 1988 and references therein; Tomeoka 1993). CI chondrites show no evidence of nebular or preaccretionary aqueous alteration (Bischoff 1998). However, there appears to be evidence to support aqueous alteration of a preaccretionary nature in the fine-grained, accretionary rims of many chondrules within CM meteorites. Most authors note the existence of a sharp boundary between the chondrules and the phyllosilicate rims (Bischoff 1998 and references therein; Ciesla et al. 2003), however Browning et al. (1994) reported the observation of a gradual coalescence of chondrule rims with surrounding CM components that was inconsistent with a nebular origin. He also noted delicate rim extensions into the adjacent matrix, which he believed would not survive incorporation into a parent body and subsequent regolith gardening (Browning et al. 1994). Browning et al. (1994) postulates that fine-grained rims in CM chondrites are the product of fluid-rock interactions, with the *in situ* precipitation of phyllosilicate rim material along fractures and interstices around dissolving olivine in an aqueous medium.

Many authors have found a disequilibrium mineralogy within the rims, in the form of numerous particles of anhydrous minerals and minerals with widely varying degrees of alteration (Bischoff 1998 and references therein). It would be unlikely that such a heterogeneous degree of alteration would be observed or that the anhydrous mineral particles would survive unaltered if the chondrules had undergone substantial aqueous alteration on a parent body (Bischoff 1998 and references therein, Ciesla et al. 2003). These authors have either invoked a nebular origin for the phyllosilicate rims or a two-stage alteration process to explain the different mineralogies, with alteration occurring both within the solar nebula and on the parent body (Bischoff 1998 and references therein).

Disequilibrium mineralogies are also found between the phyllosilicates of CAIs and the phyllosilicates within the surrounding material. Schirmeyer et al. (1997) found enriched levels of Li within the phyllosilicates of CAIs, but did not detect any Li in phyllosilicates of the adjacent matrix. They suggested that the phyllosilicates found within the CAIs formed by alteration in the nebula prior to incorporation into the parent body, where additional aqueous alteration occurred to produce the phyllosilicates found in the matrix (Shirmeyer et al. 1997).

CR Chondrites. In contrast to CM chondrites, CR chondrites do not appear to be breccias (Bischoff 1998). Therefore, aqueous alteration found in individual components, such as dark inclusions, is assumed to have occurred prior to accretion of the parent body (Bischoff 1998). The dark inclusions of CR chondrites have been found to contain higher amounts of phyllosilicates than the matrix, suggesting a nebular origin (Zolensky, et al. 1992). Ichikawa & Ikeda (1995) found the chemical composition of chondrule phyllosilicates different from matrix phyllosilicates in the CR chondrite Yamato-8849. They also noted a sharp boundary between chondrule phyllosilicates and matrix phyllosilicates (Ichikawa & Ikeda 1995). Similarly, Ichikawa & Kojima (1996) found a sharp boundary between chondrule glass and surrounding phyllosilicates in the CR chondrite Y-790112.

In their study of the CR2 meteorite, Al Rais, Zolensky et al. (1996) found spherules ranging from glassy to serpentine-rich. The authors suggest that these may be preaccretionary objects exhibiting progressive stages of aqueous alteration (Zolensky et al. 1996). It was later found that the spherules show deuterium excesses (Guan & Zolensky 1997), which the authors attribute to nebular alteration by D-enriched, interstellar water.

CV Chondrites. Considerable amounts of phyllosilicates have been identified in the CV3 chondrites Bali, Grosnaja, Kaba, and Mokoia, while much smaller amounts have been

found in Allende and Vigarano (Krot et al. 1995).

In the CV3 chondrite, Mokoia, Tomeoka (1993) found that the phyllosilicate content differs within clasts and among clasts, indicating aqueous alteration must have preceded some brecciation events. He reasons that the small size of the olivines in the matrix of Mokoia should make them more permeable to fluids, hence more reactive to aqueous alteration than the olivines and pyroxenes in the chondrules (Tomeoka 1993). This should result in a greater degree of alteration in the matrix than in the chondrules, yet the opposite is observed (Tomeoka 1993). Tomeoka (1993) concludes that the observations suggest that some chondrules, inclusions, and portions of the matrix of Mokoia experienced aqueous alteration prior to incorporation into the parent body.

In Allende, phyllosilicates are found only within the CAIs (Bischoff 1998; Krot et al. 1995), which most authors attribute to a nebular origin (Bischoff 1998). Veins within the dark inclusions of Allende have been attributed to "dehydrated phyllosilicates" (Krot et al. 1995). It has been suggested that these features of the dark inclusions resulted from the dehydration of phyllosilicates during asteroidal metamorphism (Krot et al. 1995 and references within) although this remains controversial (Weisberg et al. 1996; Weisberg & Prinz 1998).

Krot et al. (1995) propose that the heavy, heterogeneous aqueous alteration in the CV3 chondrite, Bali, occurred on an asteroid. They conclude that all of the secondary processes of CV3 chondrites are correlated occurrences and may have a related origin, which they determine to be alteration on a parent body (Krot et al. 1995). Alternatively, Bischoff (1998) believes on the basis of observations of the phyllosilicates in CV3 chondrites, that those found within CAIs are more likely the result of nebular processes and those found within the matrix are more likely the result of parent body processes.

Mechanisms for Nebular Alteration. Bischoff (1998) points out that many of the features identified in chondrites would be difficult to explain without taking into account preaccretionary aqueous alteration. In the past, however, the production of phyllosilicates in the solar nebula was believed to be kinetically inhibited (Prinn & Fegley 1987). Prinn & Fegley (1987) later presented a model that demonstrated that phyllosilicates could form in a giant planet "subnebula", due to increased water vapor pressure.

Recently, Ciesla et al. (2003) presented an alternative model for the nebular production of phyllosilicates that result in the fine-grained, accretionary rims of chondrules. As previously noted, the kinetic inhibition to phyllosilicate production can be overcome in areas where the water vapor pressure is enhanced. Rather than invoking a giant planet subnebula, the model of Ciesla et al. (2003) calls for a "chondrule-forming" shock to raise the water vapor pressure. Shocks within the solar nebula are now generally believed to be the mechanism necessary to form chondrules (Connolly & Love 1998; Ida et al. 2001; Desch & Connolly 2002; Ciesla & Hood 2002; Connolly & Desch 2004; Desch et al. 2005). In this case, a shock propagating at $\sim$ 5 km/s occurs in an area of the solar nebula beyond the snow line in which the amount of water ice is enhanced by many orders of magnitude. Ice particles ahead of the shock front are vaporized due to radiation from hot particles immediately behind the shock, thereby raising the water vapor pressure. As the shock progresses through the area of enhanced water vapor pressure, compression raises the partial pressure of water even further, resulting in a faster rate of phyllosilicate production and an increased phyllosilicate stability temperature. Their model shows that the amount of time before ice reforms is $\sim$ 12 days, during which time phyllosilicate grain sizes comparable to those observed in the fine-grained rims of chondrules are achieved (Ciesla et al. 2003).

2.2. *Protoplanetary Disks*

Protoplanetary disks are rotating disks of gas and dust surrounding a protostar or pre-main-sequence (PMS) star, from which planets may eventually form. We base our understanding of protoplanetary disks on the single example presented by our own Solar System, theoretical models, and the observations of disks surrounding other stars.

Theory tells us that the initial stage of star formation involves the gravitational collapse of a slowly rotating molecular cloud core resulting from the loss of magnetic and turbulent support (de Pater & Lissauer 2001; Shu et al. 1987). Although the rotation of the cloud core is small, nevertheless it still contains too much angular momentum for all of the material to collapse to a single star (Podosek & Cassen 1994; de Pater & Lissauer 2001). This results in the formation of a flattened, nebular disk surrounding the growing protostar which retains most of the angular momentum of the system (de Pater & Lissauer 2001; Shu et al. 1987). In our Solar System, for example, even though the Sun contains 99.8% of the mass, over 98% of the angular momentum is in the orbits of the planets, which represent what remains of the solar nebula (de Pater & Lissauer 2001). In isolated, low-mass stars of $< 2\ M_{\odot}$, the mass infall is eventually halted by stellar winds (Shu et al. 1987). These stellar winds are produced after the conversion of gravitational energy to kinetic energy during collapse leads to an increase in temperature, causing deuterium burning, which, in turn, leads to convection and the development of a dynamo and magnetic field (Shu et al. 1987). Shu et al. (1987) describe four basic stages of star formation: 1) formation of a slowly rotating cloud core, 2) collapse of the cloud core to a central protostar and disk, both embedded within an infalling envelope of gas and dust, 3) disk accretion onto the central protostar giving rise to bipolar outflows, and 4) a T Tauri star with remnant disk.

The infall stage for solar-like stars is estimated to last $\sim 10^5$ to $\sim 10^6$ years (Podosek & Cassen 1994; de Pater & Lissauer 2001) (essentially the free-fall time), resulting in a rotationally-supported nebular disk with an initial composition the same as the pressure-supported protostar (de Pater & Lissauer 2001). The infall stage is followed by disk evolution and clearing (de Pater & Lissauer 2001), leaving an isolated PMS or main-sequence star (Adams et al. 1987).

Disk Lifetimes. The lifetimes of protoplanetary disks, including the solar nebula, and the mechanism for clearing are poorly understood (Podosek & Cassen 1994; de Pater & Lissauer 2001). Mechanisms that have been suggested include mass accretion onto the central star, clearing by solar wind during the T Tauri phase and photoevaporation (Hartmann 1998a; de Pater & Lissauer 2001). Mass accretion is expected to be the most important method for disk clearing, with median mass accretion rates for T Tauri stars $\sim$ 1 Myr old of $\dot{M} = 10^{-8}\ M_\odot\ \mathrm{yr}^{-1}$ (Hartmann 1998b). (Mass accretion rates for stars in the FU Orionis stage are expected to be even greater, at $\dot{M} = 10^{-6}$ to $10^{-5}\ M_\odot\ \mathrm{yr}^{-1}$). The lifetimes of protoplanetary disks around solar-type stars are not only constrained by astronomical observations of disks surrounding such stars, but also by the evidence found within residual materials of the solar nebula, as there is no reason to believe that the Solar System is unique.

Observations reveal that disks are both common and normal (Podosek & Cassen 1994; Hillenbrand et al. 1998; Kenyon 2002) and that the youngest protoplanetary disks have ages $\lesssim 10^7$ yr (Podosek & Cassen 1994; de Pater & Lissauer 2001). In their study of disk frequencies and lifetimes in young clusters, Haisch et al. (2001) found an overall disk lifetime of ~ 6 Myr. They found cluster disk fractions were initially high ($\geq 80\%$), rapidly decreasing with cluster age, resulting in one-half of the cluster stars losing their

disks $\leq$ 3 Myr, although some disks remain for $\sim$ 10 Myr. An earlier study by the same authors indicated a correlation between disk lifetimes and stellar mass, with high-mass stars losing their disks faster than lower mass stars. Age determination of stars and clusters is itself problematic, with errors of up to a factor of two possible (Podosek & Cassen 1994). Taking this into account, Haisch et al. (2001) calculated that their determined overall disk lifetime may be as low as 4 Myr.

Knowledge of the lifetimes of disks is key to understanding the time during which disk evolution and nebular processing of materials occurs. Isotopic data from meteorites, in some cases, suggest that nebular processing proceeded for $\geq 10^7$ years (Podosek & Cassen 1994). Using absolute dating of U-Pb/Pb-Pb and relative dating of ^{26}Al and ^{87}Sr/^{86}Sr, it has been found that basaltic achondrites, chondrules, and some inclusions require several million years (Podosk & Cassen, 1994). Chondrule ages have been determined using the short-lived radionuclides ^{53}Mn, ^{26}Al, and ^{129}I (Wadhwa & Russell 2000). This has resulted in a formation age for most chondrules of at least a few Myr after CAIs, which formed $\sim$ 4.566 Gyr ago. Additionally the "ages" of chondrules span several million years, leading to the conclusion that the solar nebula had a lifetime of at least $\sim$ 3 Myr and possibly as long as $\sim$ 10 Myr, consistent with observations of extrasolar disks (Wadhwa & Russell 2000).

Disk Evolution. Basic equilibrium condensation models tell us that 1-2% of solar nebular material would exist in solid form at sufficient distances from the central protosun, with silicates and metal-rich condensates located throughout the disk and ice located only in the outer parts. However, the presence in meteorites of disequilibrium compounds and pre-solar grains show that these equilibrium condensation models are too simplistic (de Pater & Lissauer 2001). At least some of this evidence seems to be the result of differing thermal histories (Woolum & Cassen 1999).

The infall stage of star formation is expected to have been very active and highly turbulent (de Pater & Lissauer 2001). High accretion rates during the early stages of infall are expected to produce extremely high midplane temperatures (Woolum & Cassen 1999). In their effort to place constraints on nebular temperatures, Woolum and Cassen (1999) modeled the midplane temperatures of 26 T Tauri stars in the terrestrial planet-forming region. They achieved estimates of temperature by combining disk accretion rates, other observed disk properties, accretion disk theory, and a simple radiative transfer model. They conclude that mature T Tauri protoplanetary disks ($\sim$ 1 Myr old) can condense the major constituents of primitive meteorites, as the temperature is not hot enough to vaporize silicates at 1 AU. At 2.5 AU all moderately volatile elements condense, including H_2O ice in about half of the cases. However, in younger disks ($\lesssim 10^5$ yr) with higher accretion rates, the temperature was high enough to result in vaporization of silicates at 1 AU, and possibly at 2.5 AU (Woolum & Cassen 1999). Woolum and Cassen (1999) point out that the presence of highly volatile elements and phases in meteorites shows that meteoritic accumulation from the solar nebula persisted to very low temperatures, including $T \leq 300$ K, at which phyllosilicates are favored thermodynamically. Based on the ages of the stars in their study, some of which are as young as 10^5 yr, and coagulation timescales, they conclude that cooling from the hot nebula phase was rapid ($\ll 10^6$ yr). Woolum & Cassen (1999) also point out that modeling shows the formation of km-sized bodies within 10^4 to 10^5 yrs, with growth beyond a radius of 5-km resulting in melting by ^{26}Al, consistent with early differentiation of parent bodies. They conclude their results would indicate that planetesimals already exist in T Tauri disks (Woolum & Cassen 1999). These disk conditions could lead to aqueous alteration of parent bodies in $\leq$ 1 Myr.

Regardless of whether phyllosilicate production occurs in the nebular environment

or on the surface of parent bodies, these results support the idea that phyllosilicates should exist in protoplanetary disks.

3. Mid-Infrared (MIR) Spectra

Observational evidence for disks around young stellar objects (YSOs) is both direct and indirect. Indirect evidence comes in the form of excess infrared (IR) emission over what would be expected from the stellar photosphere alone (McCaughrean & O'Dell 1996; Adams et al. 1988; Chiang & Goldreich 1997, and references therein; de Pater & Lissauer 2001). Lynden-Bell & Pringle (1974) proposed that the excess IR emission was the result of disk accretion, as opposed to a uniform (spherical) circumstellar shell of dust, and Rucinski (1985) presented the argument that dusty disks were the only tenable explanation for IRAS (Infrared Astronomical Satellite) observations. It is now generally believed that the excess IR emission is the result of thermal emission due to reprocessed starlight from circumstellar dust grains, rather than disk accretion (Adams et al. 1988; Hartmann 1998b). Fluxes ($\frac{3}{8\pi}\,\dot{M}\,\Omega^2$) from steady state accretion in T Tauri stars ($\dot{M} \lesssim 10^{-8}\,M_\odot\,yr^{-1}$) produce an effective temperature which is much less than that which would be seen if accretion dominated the flux ($T \ll T \propto r^{-3/4}$), and are nearly indistinguishable from purely reprocessing disks ($T \propto r^{-1/2}$). This leads to the conclusion that during the T Tauri stage, the system consists of a passive, reprossesing disk, in which the excess infrared emission originates from dust grains in the outer layers of the disk that are heated by starlight (Kenyon & Hartmann 1987). Direct observations of disks come from both millimeter data and Hubble Space Telescope (HST) images (McCaughrean & O'Dell 1996; de Pater & Lissauer 2001). Millimeter data have suggested disk masses from $\sim$ 0.001 - 0.1 $M_\odot$ (note that the minimum-mass solar nebula (Weidenschilling 1977), 0.01 - 0.07 $M_\odot$, falls within this range). HST images

reveal disks around some young stars extending out to $\sim$ 100 AU (de Pater & Lissauer 2001). De Pater and Lissauer (2002) note that IR excess emission is observed in 25-50% of pre-main-sequence stars of 1 $M_{\odot}$. In the Trapezium Cluster, McCaughrean & O'Dell (1996) argue that the lower limit to stars with disks is probably $\geq$ 30% and that 50% is reasonable.

The spectra of young stellar objects with IR excess emission contain information about the composition of the circumstellar dust which gives rise to that emission. While observations at millimeter wavelengths probe closer to the midplane of the disk, mid-infrared observations probe the surface layers of the disk. Due to observation of silicate emission bands, the exterior is believed to consist of submicron to micron-sized particles (Chiang 2004). The spectra of YSOs, such as T Tauri and Herbig Ae stars, routinely exhibit such silicate emission bands at $\lambda \sim 10$ μm and ~ 20 μm. This implies that grains are emitting in the Rayleigh limit, $a \leq \lambda/2\pi$ (Chiang 2004), as the observed silicate feature would diminish if the particle size was more than a few microns (Pollack 1994; Nakamura 1998). The silicate features observed in the spectra of protoplanetary disks allow us to explore the mineralogy of the dust, including the possible contribution of emission from phyllosilicates.

3.1. *MIR Spectra of Silicates*

In general, silicates are SiO_4 tetrahedral structures with the oxygen atoms at each corner and the Si atom in the center (Sitko et al. 2000; Krishna Swamy 2005). The characteristic mid-infrared silicate feature at ~ 10 μm is due to the Si-O vibration mode, whereas the ~ 20 μm feature is due to the Si-O-Si bending mode (Jäger et al. 1994; Sandford 1996; Sitko et al. 2000). These features are seen in both absorption and emission (Jäger et al. 1994; Sandford 1996). Whether they are seen in absorption or emission depends on optical depth

and grain temperatures. Amorphous (glassy) silicates produce broad (varying over $\sim$ 0.5 - 1 μm), smooth spectral profiles (Jäger et al. 1994; Krishna Swamy 2005). Crystalline silicates show substructure with sharp (varying over $\leq$ 0.05 μm) and distinct features that vary from mineral to mineral (Sandford 1996; Jäger et al. 1998; Krishna Swamy 2005). These features are much more prominent in the 20-40 μm region than in the 10 μm region.

The silicate band positions and profiles are highly diagnostic of stoichiometry (Dorschner et al. 1995; Fabian et al. 2001; Krishna Swamy 2005). Laboratory data show a correlation between the Mg/Fe ratio and band position (Jäger et al. 1998; Krishna Swamy 2005), with band position shifting to longer wavelength with increasing iron content (Fabian et al. 2001; Krishna Swamy 2005). Mg-rich crystalline olivine exhibits a distinct feature at 69.7 μm that is not present in Fe-rich silicates. With just 10% Fe, this feature shifts to 72.9 μm (Krishna Swamy 2005). Diagnostic features in amorphous silicates, indicative of FeO content, include position of peak wavelengths, band strengths, band widths (FWHM), 20 μm /10 μm ratio, the depth and profile of the trough between the $\sim$ 10 μm and $\sim$ 20 μm bands, and the occurrence of minor bands (Dorschner et al. 1995). Distinctive features at 1 μm and 2 μm can distinguish between olivines and pyroxenes (Jäger et al. 1994; Dorschner et al. 1995). Other spectral features are indicators of particle shape (Fabian et al. 2001).

3.2. *MIR Spectra of Phyllosilicates*

Phyllosilicates exhibit the characteristic $\sim$ 10 μm and $\sim$ 20 μm features, with distinctive substructure particular to each specific mineral. All phyllosilicates also show a distinct absorption feature at 6 μm due to H_2O . Although the narrow spectral features of phyllosilicates are unique to each mineral, Calvin & King (1997) found overall differences

between the Mg-rich and Fe-rich phyllosilicates. They measured diffuse reflectance from 0.3-25 μm of Mg-bearing and Fe-bearing phyllosilicates in an effort to bracket the composition of phyllosilicates found in CI and CM meteorites. In their samples of Mg-rich phyllosilicates, they saw a strong hydroxyl absorption near 2.3 μm and features at 1.4 and 2.0 μm due to OH and Mg-OH vibrational overtones. The 1.4 and 2.0 μm features were very weak or completely lacking in the Fe-rich samples. Extremely strong peaks were found at $\sim$ 10, 15, and $>$ 20 μm in the Mg-rich phyllosilicates, which were not seen in the Fe-rich phyllosilicates (Calvin & King 1997).

The unique and distinctive mid-infrared spectral features of silicates, in general, and phyllosilicates, in particular, make the study of the mineralogy of protoplanetary disks possible.

4. Instrumentation

There are several space-based and ground-based mid-infrared instruments in operation or in the planning stages. Here I will examine the wavelength coverage of some examples of each, their spectral resolution, and their sensitivity. Spectral resolution is given by $R = \lambda/\Delta\lambda$, where $\Delta\lambda$ is the smallest difference in wavelength that can be distinguished at a particular wavelength, λ. For example, for $\Delta\lambda = 0.17$ nm at 1000 nm, $R \sim 5900$. Sensitivity is a measure of the minimum flux detectable during a given integration time.

4.1. *Space-based Instruments*

Infrared Space Observatory. Although no longer in service, the Infrared Space Observatory (ISO) bears mentioning, due to the availability of archived data. Operational between November, 1995 and May, 1998, ISO covered the wavelength range 2.5-240 μm.

ISO's short-wave spectrometer, SWS, had coverage over 2.4-45 μm , with spectral resolution, $R = 1000$. LWS, the long-wave spectrometer covered 45-196.8 μm with $R = 150$-200. ISO's sensitivity was reported at 60 μJy at 10 μm and 600 μJy at 60 μm for a 1000s integration time (Kessler 1991; Kessler 2002; ISO 2006).

Spitzer Space Telescope. The Spitzer Space Telescope launched August 25, 2003 and is expected to stay in service until at least 2008. The Infrared Spectrograph (IRS) aboard Spitzer covers the wavelength range of 5.2-38 μm , with $R \sim 60$-120 overall. For 9.9-37.2 μm , $R \sim 600$. At low-resolution, the 1σ sensitivity for a 512-second integration time is 0.06 mJy and 0.4 mJy, for 6-15 μm and 14-38 μm, respectively. For high-resolution, the sensitivity is 2.7 x 10^{-19} W/m^2 and 8.5 x 10^{-19} W/m^2 for the same wavelengths and integration time (Spitzer 2004).

James Webb Space Telescope. The James Webb Space Telescope (JWST) will be launched no sooner than 2013 and will include the Mid-Infrared Instrument, or MIRI. MIRI will cover the wavelength range of 5-29 μm , with spectral resolution of $R = 3000$. Expected 10σ sensitivity for a 10,000s integration time is 1.2 x 10^{-20} W/m^2 at 2.4 μm and 5.6 x 10^{-20} W/m^2 at 22.5 μm (JWST 2006).

4.2. *Atmospheric-based Instruments*

Stratospheric Observatory for Infrared Astronomy. The Stratospheric Observatory for Infrared Astronomy, or SOFIA, is the successor to the Kuiper Airborne Observatory, which flew from 1971 to 1995. SOFIA, a 2.5 meter reflecting telescope aboard a Boeing 747SP, is scheduled for Operations Readiness Review in the Fall of 2006. Full operations are expected in Fall, 2009. The Echelon-Cross-Echelle Spectrometer (EXES) aboard SOFIA will cover the 5-28 μm wavelength range, with $R = 10^5$ for high-resolution, $R = 10^4$ for

medium-resolution, or $R = 3000$ for low-resolution. The 4σ sensitivity for a 900s integration time for high, medium, and low-resolution at 10 μm is $\sim$ 1.3 Jy, $\sim$ 0.4 Jy, and $\sim$ 0.2 Jy respectively, and at 20 μm is $\sim$ 2.7 Jy, $\sim$ 0.9 Jy, and $\sim$ 0.5 Jy (SOFIA 2006).

4.3. *Ground-based Instruments*

Gemini North. Michelle, a mid-infrared spectrometer and imager, covering the wavelength range of 7-26 μm , formerly available at UKIRT (United Kingdom Infrared Telescope) is now available for use at Gemini North. Spectral resolution values are as follows (Michelle 2006):

- $R \sim 200$ for 7-14 μm (low-resolution)
- $R \sim 110$ for 16-26 μm (low-resolution)
- $R \sim 1000$ for 7-26 μm (medium-resolution)
- $R \sim 3000$ for 7-26 μm (high-resolution)
- $R \sim$ 10000-30000 for 7-22 μm (echelle high-resolution)

5σ sensitivities for a one-hour integration time are as follows:

- 14 mJy at 10.5 μm , low resolution
- 21 mJy at 9.0 μm , medium resolution
- 270 mJy at 9.0 μm , high resolution

The Texas Echelon Cross Echelle Spectrograph (TEXES) will be available for use at Gemini in November, 2006 as a visitor instrument. TEXES will cover the 5 - 25 μm wavelength range, with resolution between 100,000 and 40,000 (with R inversely

proportional to wavelength for the 10-25 μm region). 5σ sensitivity for a one-hour integration time is measured at 0.48 Jy at 10 μm and 0.57 Jy at 17 μm (TEXES 2006).

Gemini South. The Thermal-Region Camera Spectrograph (T-ReCS) covers the wavelength range between 8 and 26 μm , with a resolution of $R = 100$ overall, and $R \sim 1000$ for 8-13 μm. 5σ sensitivities for one-hour integration times are 2.2 mJy at 10.3 μm , 1.4 mJy at 9.8 μm , and 21 mJy at 18.06 μm (T-ReCS 2006):

Subaru. The Cooled Mid-Infrared Camera and Spectrograph at the Subaru telescope spans the 7.5-25 μm region, with $R \sim 2500$. 1σ spectral sensitivity for 1s integration time is 340 mJy (NL grating) and 2500 mJy (NM grating) for 7.8-13.3 μm and 3000 mJy for 16.7-20.7 μm (COMICS 2006).

NASA Infrared Telescope (IRTF). MIRSI, the Mid-Infrared Spectrometer and Imager, at IRTF covers the wavelength range 2-28 μm , with $R = 200$ at 10 μm and $R = 100$ at 20 μm. 1σ sensitivities for a 60s integration time are 20 mJy at 10 μm and 100 mJy at 20 μm (MIRSI 2006).

5. Outline of Thesis

In the following chapters I will discuss the minerals that we should expect to find in protoplanetary disks. For those minerals of interest I will describe methods of determining the complex index of refraction for use in Mie theory in order to model the spectra of the disks. I will detail the key results achieved through the use of Mie theory, and the various theoretical methods used to account for non-spherical particles.

A refresher on radiative transfer will be presented, including emission from both optically thin and optically thick slabs. Applications to debris disks and the zodiacal light will be discussed. The disk model of Chiang & Goldreich (1997) will be described, including

the physical basis for their model. I will explain the radiative transfer code I have developed, based on the Chiang & Goldreich model, in order to produce theoretical spectral energy distributions (SEDs) of protoplanetary disks of varying mineralogies. I will present the modeled SEDs with and without the inclusion of 3% phyllosilicates. From these results, the determination will be made as to whether phyllosilicates can be detected in extrasolar protoplanetary disks using the instruments available. Finally, the implications of detection or non-detection of phyllosilicates will be addressed.

CHAPTER 2

OPACITIES

A knowledge of the minerals we should expect to find in protoplanetary disks, and the basis for those expectations, is paramount to this work. In order to accurately model the spectral energy distribution (SED) of protoplanetary disks to compare to observations, it will be necessary to possess a thorough knowledge of these minerals, along with an understanding of and competency in the methods used to determine the unique mid-infrared emission features of each mineral species considered.

1. Minerals of Interest

The dust in protoplanetary disks is expected to consist primarily of compounds of the rock-forming elements (Si, O, Fe, Mg, Al, Ca, Na, Ni) along with carbonaceous compounds. Based on cosmic element abundances, the most abundant species should be compounds of Si, O, Mg, and Fe, plus carbon dust (Gail 2003). The silicates found in the disk are expected to be largely amorphous initially, since crystalline silicates are not detected in the molecular clouds from which the disks form (Gail 2003). The silicate feature of the interstellar medium (ISM) is broad and featureless, showing little structure, leading to the conclusion that the most common silicates in astrophysical objects are amorphous (Sandford 1996; Draine 2003; Krishna Swamy 2005). Kemper (2004) concluded that $< 5\%$ mass fraction of the ISM was crystalline. However, amorphous silicates are only metastable and susceptible to annealing processes even at relatively low temperature (Sandford 1996). (Annealing is the process in which the long-range ordered arrangement of the silicate tetrahedra is brought about by atomic diffusion, converting amorphous silicates to crystalline silicates [Krishna Swamy 2005]). Consequently, silicates are expected to be an amorphous non-equilibrium mixture in the outer portions of the disk, progressing through a crystalline non-equilibrium mixture in the middle portion of the disk, to a crystalline equilibrium mixture in the inner portion or

the disk (Gail 2003). In fact, the spectra of many pre-main sequence stars observed require the presence of crystalline silicates (Waelkens et al. 1996; Meeus et al. 2001). Therefore any study of disks must consider both amorphous and crystalline silicates.

1.1. *Outer Disk*

Pollack et al. (1994) estimated the dust composition of molecular cloud cores (from which protoplanetary disks are formed) and the cold outer regions of accretion disks around young stellar objects. Their estimates are based on astronomical observations and theory, the chemical composition of primitive bodies in the Solar System (chondrites, IDPs, asteroids, and comets), and laboratory measurements of optical constants of key grain species. They found the cloud cores consisted primarily of amorphous olivine and orthopyroxene, with lesser amounts of troilite (FeS), metallic iron, organics, and H_2O ice. They reached this conclusion as follows (Pollack et al. 1994).

Silicates. The silicate composition arrived at by Pollack et al. was built upon results from studies of refractory cometary grains, especially those of Bregman et al. (1987) who fit the 9.7 μm feature of the coma of comet Halley with fractional abundances of 60% olivine and 40% pyroxene. In the Pollack et al. (1994) model, a combination of olivine and orthopyroxene was assumed. The relative abundances of each were determined based on solar chemical abundances and stochiometry. In addition a Fe/(Fe+Mg) ratio of 0.3 was assumed, consistent with the measured average ratio of the coma of comet Halley and chemical and mineralogical analysis of anhydrous, chondritic IDPs with apparent cometary sources (Pollack et al. 1994).

Troilite (FeS). UV observations of the diffuse ISM indicate that up to 75% of the cosmic abundance of S is bound in refractory materials. Thermodynamic equilibrium cal-

culations of a cosmic mixture result in FeS as the primary S-bearing mineral. Fe-rich sulfide grains are the most abundant S-bearing mineral in cometary-derived anhydrous, chondritic IDPs. Additionaly, troilite and stoichiometrically similar minerals are the dominant carriers of S in ordinary chondrites (Pollack et al. 1994).

Metallic Iron. Although most of the Fe in the Pollack et al. (1994) model is contained in silicates and troilite, they assumed the remaining $\sim$ 20% is in the form of metallic iron based on the occurence in IDPs, cometary refractory grains (Halley), and ordinary chondrites.

Organics. It has been determined that most refractory carbon is in forms other than graphite, as a mere 10% of the cosmic abundance of C will produce observed spectral features of the diffuse ISM if graphitic. Refractory organic matter, or CHON particles (dust particles rich in C, H, O, and N) found in the coma of comet Halley are believed directly inherited from the outer solar nebula. Refractory organic compounds are the chief C-containing species in IDPs and carbonaceous chondrites, such as the kerogen found in the Murchison meteorite. Pollack et al. (1994) estimated that $\sim 60\% \pm 15\%$ of the carbon in molecular clouds is contained in organic grains, with the balance in a more volatile component, such as methanol.

H_2O ice. The $\sim$ 3 μm feature of H_2O ice is seen in the infrared spectra of molecular clouds. It has been estimated that, within a factor of two, $\sim$ 10% of the oxygen in molecular clouds is found in H_2O ice, with the majority of the O contained in silicates (Pollack et al. 1994).

Pollack et al. (1994) concluded that the composition in the cold outer regions of protoplanetary disks would be the same as the parent molecular cloud with the following exceptions:

- Elevated H_2O ice, with $\sim$ 50% of O contained in H_2O ice, consistent with the abundance observed in Solar System comets.
- Si gas contained in the parent molecular cloud would be converted to solid SiO_2 (quartz) in the disk.
- FeS would increase to contain 75% of the cosmic abundance of S, where metallic iron would decrease to 10% of the cosmic abundance of Fe.

Table 2. Mass fractions of the most abundant grain species in disks

	Mass Fraction	
	Molecular Cloud	Disk
metallic iron	2.53 x 10^{-4}	1.26 x 10^{-4}
olivine	2.51 x 10^{-3}	2.64 x 10^{-3}
orthopyroxene	7.33 x 10^{-4}	7.70 x 10^{-4}
troilite	5.69 x 10^{-4}	7.68 x 10^{-4}
refractory organic	3.53 x 10^{-3}	3.53 x 10^{-3}
volatile organic	6.02 x 10^{-4}	6.02 x 10^{-4}
water ice	1.19 x 10^{-3}	5.55 x 10^{-3}

Table 2 shows grains species and properties of the Pollack et al. (1994) grain model.

Gail (2003, 2004) used the grain model of Pollack et al. (1994) to arrive at an outer disk composition of amorphous olivine, pyroxene, and quartz, solid iron and troilite, and kerogen. Kerogen was chosen as representative of the carbon-rich component of Pollack et al., as it is the carbonaceous material found in the matrix of carbonaceous chondrites (Gail 2003). The relative abundances of these species are shown in Table 3.

Table 3. Dust composition in the outer disk.

Species	Mg	Fe	Si	S	C
olivine-type	0.83	0.42	0.63		
pyroxene-type	0.17	0.09	0.27		
quartz-type			0.10		
iron		0.10			
troilite		0.39		0.75	
kerogen					0.55

1.2. *Inner Disk*

Estimates have been made of the composition of dust species found in the inner disk regions based on calculations of vaporization and annealing of grains transported inward into areas of higher temperature during the viscous phase of the protoplanetary disk, in addition to astronomical observations (Gail 1998, 2003, 2004; Bouwman, 2001; Wehrstedt & Gail, 2003; van Boekel et al. 2004; Schütz et al. 2005). Gail (1998) found annealing of silicates occurs at $\sim$ 800 K in 10^{12} s, resulting in the conversion of the silicates from amorphous to crystalline. In their discussion of nebular shocks, Hallenbeck et al. (2000) determined that a 1 μm silicate grain is annealed within ten minutes at temperatures $\geq$ 1000 K. However, compounds of Al and Ca can survive at much higher temperatures than Mg-Fe-Si compounds, leading to the survival of species like corundum (Al_2O_3) in regions where silicates do not (Gail 1998).

Gail (1998, 2003, 2004) estimates the composition of the inner regions of the disk consist of pure, crystalline forsterite (Mg_2SiO_4) and enstatite ($MgSiO_3$), with the innermost regions iron and carbon-free, yet containing an aluminum component. Corundum was chosen as representative of the aluminum component, consistent with the discovery of a $\sim$ 0.2 μm presolar grain in the carbonaceous chondrite Acfer 094 corresponding to either

corundum or hibonite ([Ca,Ce][Al,Ti,Mg]$_{12}$O$_{19}$) (Nagashima et al. 2004). Nagashima et al. (2004) also found a $\sim$ 1 μm presolar grain of Mg-olivine (forsterite) in Acfer 094. Five more grains of amorphous silicate material, consistent with forsterite or enstatite, were found; two in Acfer-094 and three in the carbonaceous chondrite NWA 530.

Condensation and chemical equilibrium models predict an innermost disk region made up of almost entirely forsterite, grading into enstatite at lower temperatures (van Boekel et al. 2001). This seems reasonable as laboratory experiments have shown that thermal annealing of amorphous silicates will gradually produce crystalline forsterite and silica (SiO_2) (Schütz et al. 2005b). In their analysis of spectral observations of three protoplanetary disks surrounding Herbig Ae stars, van Boekel et al. (2001) observed such a gradient. In their spatially-resolved observations of β Pictoris, Okamoto et al. (2004) found crystalline silicates and micron-sized amorphous silicates concentrated at the center of the disk with submicron amorphous silicates located at greater distances from the star.

Bouwman et al. (2001) studied spectral observations of disks surrounding 14 Herbig Ae/Be stars. They were able to fit the 8.6 μm , 9.8 μm , and 11.3 μm features with SiO_2, submicron-sized amorphous olivine, and micron-sized amorphous olivine plus forsterite, respectively (Bouwman et al. 2001). Schütz et al. (2005a) fit the spectra of eight PMS objects with polycyclic aromatic hydrocarbons (PAHs), amorphous olivine (0.1-2.0 μm grains), crystalline Mg-forsterite and enstatite, and quartz.

1.3. *Minerals Considered in this Work*

Based on the above, the minerals considered in this study include both amorphous and crystalline olivines and pyroxenes (forsterite and enstatite), troilite (FeS), quartz (SiO_2), hibonite ($CaAl_{12}O_{19}$), and the phyllosilicates most commonly found in meteorites (saponite,

serpentine, montmorillonite, and chlorite). Hibonite was chosen as representative of the aluminum component of the inner disk, owing to the availability of a more complete set of optical constants than for corundum, and the fact that hibonite has been found in a number of meteorites (Steele 1995; Krot et al. 2001; Bischoff & Srinivasan 2003; Simon & Grossman 2003).

2. Extinction, Scattering, and Absorption Properties

In order to properly model and interpret the spectral energy distributions of protoplanetary disks, it is necessary to understand how the small dust particles in the surface layers of the disk interact with the radiation received from the central star. In the discussion to follow, I consider the case in which the particles are small compared to the wavelength of radiation (within the Rayleigh limit). This is the appropriate situation needed to produce an observable mid-infrared silicate feature (Pollack 1994; Nakamura 1998).

Dust particles in an accretionary disk of a young stellar object will result in the extinction of radiation emitted by the protostar. Extinction is the difference between the emitted and detected radiation and is the sum of both the radiation absorbed and the radiation scattered by the intervening particles. Extinction is highly dependent on the size, shape, and chemical composition of the particles (Bohren & Huffman 1983; Min et al. 2003). The extinction, scattering, and absorption properties of homogeneous spherical particles can be determined extremely accurately utilizing Mie theory. More realistic shapes representative of the dust in protoplanetary disks require more complicated methods.

2.1. *Homogeneous Spheres*

Following the approach of Bohren & Huffman (1983), the cross section for extinction for homogeneous spheres within Rayleigh Limit is given by

$$C_{ext} = C_{abs} + C_{sca}, \tag{2.1}$$

and the cross sections for absorption and scattering by

$$C_{abs} = \frac{W_{abs}}{I}, \tag{2.2}$$

$$C_{sca} = \frac{W_{sca}}{I}, \tag{2.3}$$

where W_{abs} is the rate at which energy is absorbed, W_{sca} is the rate at which energy is scattered, and I is the incident irradiance. The efficiencies (or efficiency factors), Q, are as follows:

$$Q_{ext} = \frac{C_{ext}}{G}, \tag{2.4}$$

$$Q_{sca} = \frac{C_{sca}}{G}, \tag{2.5}$$

$$Q_{abs} = \frac{C_{abs}}{G}, \tag{2.6}$$

where G is the geometric cross section. $G = \pi a^2$ for a sphere of radius a.

For homogeneous spheres, in the Rayleigh limit of long wavelength, where $x = \frac{2\pi a}{\lambda} \ll 1$ (λ being the wavelength of incident radiation) and m is the complex index of refraction $(n + ik)$ of the material, the efficiencies determined by Bohren and Huffman (1983) are

$$Q_{ext} = 4x \text{ Im}\left\{\frac{m^2-1}{m^2+2}\left[1 + \frac{x^2}{15}\left(\frac{m^2-1}{m^2+2}\right)\frac{m^4+27m^2+38}{2m^2+3}\right]\right\} + \frac{8}{3}x^4 \text{ Re}\left\{\left(\frac{m^2-1}{m^2+2}\right)^2\right\}, \tag{2.7}$$

$$Q_{sca} = \frac{8}{3}x^4\left|\frac{m^2-1}{m^2+2}\right|^2. \tag{2.8}$$

In the limit, where $|m|\,x \ll 1$ (still within the Rayleigh limit), the efficiency for absorption is

$$Q_{abs} = 4x \text{ Im}\left\{\frac{m^2-1}{m^2+2}\right\}\left[1 - \frac{4x^3}{3} \text{ Im}\left\{\frac{m^2-1}{m^2+2}\right\}^2\right]. \tag{2.9}$$

In the limit of long wavelength, where **both** $x \ll 1$ and $|m|\,x \ll 1$, the efficiency for absorption is then

$$Q_{abs} = 4x \text{ Im}\left(\frac{m^2-1}{m^2+2}\right). \tag{2.10}$$

In the electrostatics approximation of Bohren & Huffman (1983) for $x \ll 1$ and $|m|\,x \ll 1$, the cross sections for extinction and scattering are

$$C_{ext} = k \, \mathrm{Im} \left(\alpha \right) , \tag{2.11}$$

$$C_{sca} = \frac{k^4}{6\pi} \left| \alpha \right|^2 , \tag{2.12}$$

where $k = \frac{2\pi}{\lambda}$, and α is the *polarizability*, or the ease with which the sphere is polarized. Equation 2.11 is only accurate if the scattering is small compared to the absorption, which gives

$$C_{abs} = k \, \mathrm{Im} \left(\alpha \right) . \tag{2.13}$$

2.2. *Ellipsoids*

For ellipsoids in the Rayleigh approximation, the cross sections for scattering and absorption, averaged over all possible orientations is (Bohren & Huffman 1983; Min et al. 2003)

$$C_{sca} = \frac{k^4 V^2}{2\pi} \, \mathrm{Im} \left(\left| \alpha_1 \right|^2 + \left| \alpha_2 \right|^2 + \left| \alpha_3 \right|^2 \right) , \tag{2.14}$$

$$C_{abs} = kV \, \mathrm{Im} \left(\alpha_1 + \alpha_2 + \alpha_3 \right) , \tag{2.15}$$

where, once again, $k = \frac{2\pi}{\lambda}$, V is the volume of the particle, and α_i, for i=1,2,3 is the polarizability per unit volume. For an ellipsoid with semi-axes, a, b, and c

$$\alpha_i = \frac{m^2 - 1}{3 + 3L_i\,(m^2 - 1)}, \tag{2.16}$$

where L_i (i=1,2,3) is a geometrical factor defined by the shape of the ellipsoid

$$L_1 = \int_0^\infty \frac{abc\;dx}{2\sqrt{(s + a^2)\,(s + b^2)\,(s + c^2)}}. \tag{2.17}$$

L_2 and L_3 are found by cyclic permutation of a, b, and c, with $L_1 + L_2 + L_3 = 1$ for all a, b, and c. For a homogeneous sphere, $L_1 = L_2 = L_3 = \frac{1}{3}$, which gives

$$\alpha_i = \frac{m^2 - 1}{m^2 + 2}. \tag{2.18}$$

2.3. *Shape Distributions*

Of course the individual dust particles in protoplanetary disks are not expected to be perfect spheres or ellipsoids. However, a statistical approach can be employed to approximate the scattering and absorption properties of a collection of irregularly shaped particles using a distribution of particles of simple shapes, such as spheroids or ellipsoids (Bohren & Huffman 1983; Min et al. 2003). Bohren & Huffman (1983) discuss a shape probability function, $\mathcal{P}(L_1, L_2)$, normalized to unity. For a collection of randomly oriented ellipsoids with the same volume, V, this results in an average cross section for absorption of

$$\begin{aligned}\langle C_{abs}\rangle &= kV \int_0^1 dL_1 \int_0^{1-L_1} dL_2 \, \mathrm{Im}\left(\alpha_1+\alpha_2+\alpha_3\right)\mathcal{P}(L_1,L_2) \\ &= kV \, \mathrm{Im}\left(\bar{\alpha}\right), \end{aligned} \tag{2.19}$$

where $\bar{\alpha}$ is the average polarizability per unit volume.

Although it can be shown that there exists a relationship between C_{abs} and C_{sca} (see Min et al. (2003) for details), C_{abs} is the component needed for the disk model outlined in this work. Therefore, in the discussion to follow, results will be presented for C_{abs} only.

Continuous Distribution of Ellipsoids (CDE). Bohren & Huffman (1983) present results for the shape distribution known as the Continuous Distribution of Ellipsoids (CDE), where ellipsoids of all shapes are equally probable. In this case, $\mathcal{P}(L_1, L_2) = 2$, resulting in the average polarizability per unit volume of

$$\begin{aligned}\bar{\alpha} &= \int_0^1 dL_1 \int_0^{1-L_1} dL_2 \; \left(\alpha_1+\alpha_2+\alpha_3\right)\mathcal{P}(L_1,L_2) \\ &= 2\frac{m^2}{m^2-1}\ln m^2 - 2. \end{aligned} \tag{2.20}$$

substituting this into 2.19, we have

$$C_{abs} = 2kV \, \mathrm{Im}\left(\frac{m^2}{m^2-1}\ln m^2\right). \tag{2.21}$$

Continuous Distribution of Spheroids (CDS). CDE is suitable for the calculation of both Q_{abs} and Q_{sca} for particles within the Rayleigh limit. However, it is much more

difficult to calculate Q_{sca} for ellipsoids than spheroids (spheroids are simply ellipsoids with two equal semi-axes). Therefore, it is important to note that outside the Rayleigh limit a Continuous Distribution of Spheroids (CDS) is more feasible for the determination of Q_{sca} than CDE (Min et al. 2003). As with CDE, CDS averages over all possible shapes, with equal probability for all L ($\mathcal{P}(L)$=1). The reader is referred to Min et al. (2003) for details.

Uniform Distribution of Spheroids (UDS). The Uniform Distribution of Spheroids (UDS) is a shape distribution consisting of a uniform distribution of oblate and prolate spheroids, with a limited domain of aspect ratios for each. Min et al. (2003) note that as the geometrical factor, L, is a function of the aspect ratio, it is not possible to find an analytic expression for $\bar{\alpha}$. They point out, however, that for a given upper limit to the aspect ratio, it is possible to numerically calculate the shape averaging of the cross sections (Min et al. 2003). Once again, the reader is referred to Min et al. (2003) for details.

Distribution of Hollow Spheres (DHS). The shape distributions discussed previously assume homogeneous particles. The Distribution of Hollow Spheres (DHS) considers porous particles, in an attempt to account for the more realistic case of particles that are inhomogeneous in composition or that contain porous inclusions. Following the treatment of Min et al. (2003), consideration is given to particles with a complex index of refraction, m, with vacuum inclusions having m =1. For a hollow spherical shell, the polarizability per unit material volume is (Min et al. 2003; van de Hulst 1957)

$$\alpha = \frac{\left(m^2-1\right)\left(2m^2+1\right)}{\left(m^2+2\right)\left(2m^2+1\right)-2\left(m^2-1\right)^2 f}, \tag{2.22}$$

where f is the fraction of the total volume of the sphere occupied by the inclusion. The total material volume of a hollow spherical shell of radius, a, is $V = \frac{4}{3}a^3\left(1-f\right)$. Combining

2.15 and 2.22 gives the average cross section for absorbtion.

$$\begin{aligned} \langle C_{abs} \rangle &= kV \, \mathrm{Im}\,(3\alpha) \\ &= 4\pi a^3 k \, \mathrm{Im}\left[\frac{(1-f)\left(m^2-1\right)\left(2m^2+1\right)}{\left(m^2+2\right)\left(2m^2+1\right) - 2\left(m^2-1\right)^2 f} \right]. \end{aligned} \tag{2.23}$$

Using the statistical approach by averaging 3α over the entire range of volume fractions f=[0,1] gives the average polarizabilty per unit material volume as

$$\begin{aligned} \bar{\alpha} &= \int_0^1 3\alpha \, df \\ &= \frac{6m^2+3}{2m^2-2} \ln\left[\frac{\left(2m^2+1\right)\left(m^2+2\right)}{9m^2} \right]. \end{aligned} \tag{2.24}$$

This gives the average cross section for absorption for the Distribution of Hollow Spheres (DHS):

$$\langle C_{abs} \rangle = kV \, \mathrm{Im}\,(\bar{\alpha}). \tag{2.25}$$

Shape Distribution Effects on Spectral Features. Min et al. (2003) performed an extensive study of the shape effects in scattering and absorption by small particles. They found that in all cases, the positions of spectral features shifted to longer wavelengths, by $\sim$1 - 2 μm , when using non-spherical particles or hollow spheres, as opposed to homogeneous spheres. The most extreme shifts were seen in UDS with an aspect ratio of 10 and DHS. CDE and CDS produced the broadest spectral features. UDS with an aspect ratio of

10 and DHS produced the best fit to the spectral features of forsterite (Mg_2SiO_4) in the 20-40μm region. All shape distributions other than homogeneous spheres matched the position of maxima from astronomical objects (circumstellar dust). Additionally, Min et al. (2003) found that non-spherical particles and hollow spheres have larger average mass absorption coefficients, leading to an overestimate of species mass when mass determinations are made assuming homogeneous spheres. In the case of the forsterite studied, the overestimate was approximately a factor of two (Min et al. 2003).

Min et al. (2003) show that, to some degree, the average absorption cross sections as functions of wavelength are indistinguishable for CDE, CDS, UDS, and DHS, within the Rayleigh limit. The similarity between elongated and flattened ellipsoids and spheroids and hollow spherical shells suggests that the absorption spectrum is largely independent of the exact shapes of the individual particles so long as averaging is performed over a wide range of shape parameters. Outside the Rayleigh limit, there is a distinct advantage to using the Distribution of Hollow Spheres, due to the comparative ease of calculation (Min et al. 2003). This advantage, along with the knowledge that DHS provided the overall best fit to the observations in the Min et al. (2003) study, has led to the determination that DHS is the most appropriate method to employ in this work.

3. Complex Index of Refraction

As shown in Section 2, C_{abs}, and therefore Q_{abs}, is a function of the wavelength-dependent complex index of refraction, $m = n + ik$. A literature search was performed to determine the availability of optical constants of the minerals of interest to this work. In particular, values for n and k for the wavelength range between $\sim$ 0.1 μm and 200 μm are needed. Although satisfactory optical constants were found for olivines and pyroxenes, the

required information on phyllosilicates was sorely lacking in the literature. Data at sufficient resolution and uniform wavelength coverage was woefully inadequate. Because of this, it was desirable to experimentally determine the necessary optical constants for the phyllosilicates in a consistent manner. To that end, a collaboration was entered into with mineralogist Timothy Glotch of the California Institue of Technology. Samples of saponite, serpentine, montmorillonite, and chlorite (clinochlore, $[Mg,Fe2+]_5Al[Si_3Al)O_{10}[OH]_8$) were provided by Joseph Michalski of Arizona State University and a cronstedtite sample was provided by Laurence Garvie, also of Arizona State University. Experimental methods and results for the minerals of interest to this work are discussed. For the phyllosilicates, comparisons between the data found in the literature and the results of Glotch et al. (in preparation) are presented.

3.1. *Amorphous Forsterite and Enstatite*

Jäger et al. (2003) measured the optical constants of amorphous enstatite and forsterite for the wavelength range 0.2-500 μm. The samples were pressed into pellets and polished to a highly reflective surface. Specular reflectance measurements were made over the entire wavelength range. In addition, small grains of the sample were suspended in KBr pellets in order to obtain transmission measurements from 0.2-25 μm. The real and imaginary parts of the complex index of relection were then calculated using Kramers-Kronig relations and the Lorentz oscillator method (Jäger et al. 2003). Figure 1 shows Q_{abs} for amorphous forsterite and amorphous enstatite as computed from n and k reported by Jäger et al. (2003). Q_{abs} was calculated for a Distribution of Hollow Spheres of radius 1 μm, using an IDL subroutine I wrote for this purpose.

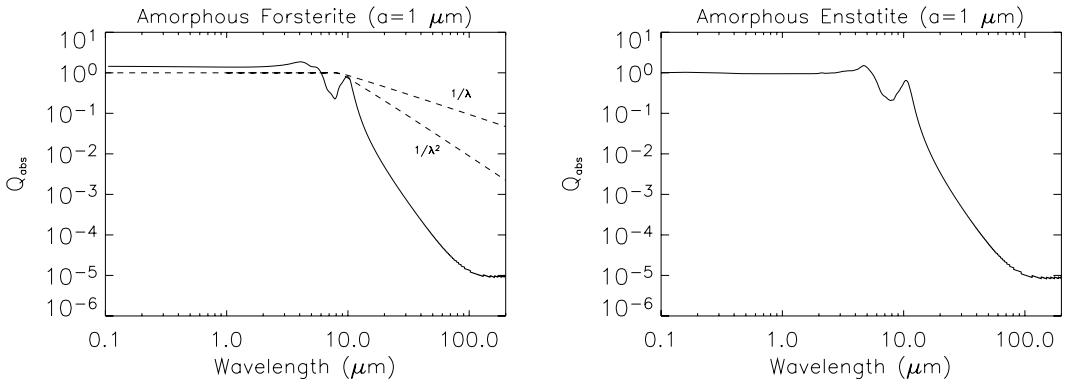

Fig. 1. — Q_{abs} for 1 μm grains of amorphous forsterite and amorphous enstatite, calculated from n and k from Jäger et al. (2003). Note that Q_{abs} decreases much more rapidly than $1/\lambda$.

3.2. *Crystalline Forsterite and Enstatite*

Jäger et al. (1998) measured the optical constants of crystalline enstatite for the wavelength range $\sim$ 2-100 μm. Once again, the samples were pressed into pellets, polished to a highly reflective surface and specular reflectance measurements made over the entire wavelength range. The real and imaginary parts of the complex index of relection were calculated using a Lorentz oscillator fit method (Jäger et al. 1998). Fabian et al. (2001) used the same methods to measure the optical constants of crystalline olivine for the wavelength range 2-200 μm. Figure 2 shows Q_{abs} for crystalline olivine and crystalline enstatite calculated for a Distribution of Hollow Spheres of radius 1 μm.

3.3. *Troilite (FeS), Quartz (SiO_2), and Hibonite ($CaAl_{12}O_{19}$)*

Optical constants for FeS, from 10-500 μm , were obtained by Begemann et al. (1994) using specular reflectance measurements. Henning & Mutschke (1997) acquired both reflectance (2-500 μm) and transmission measurements (2-25 μm) of SiO_2. Both components

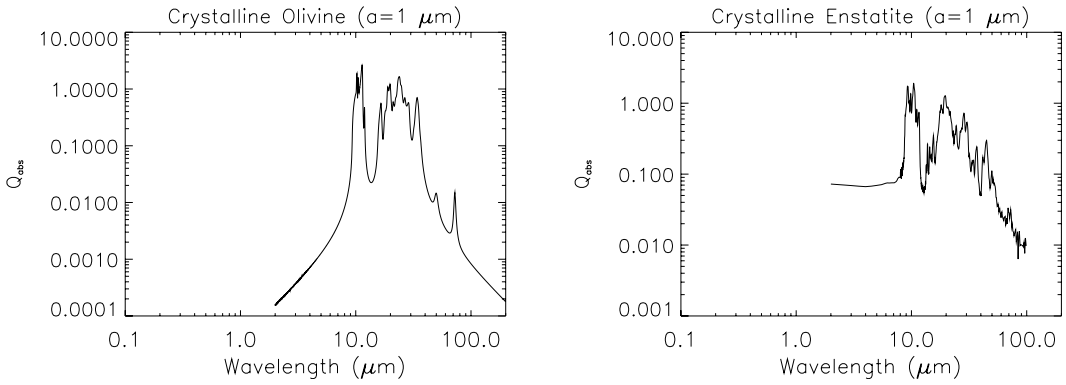

Fig. 2. — Q_{abs} for for 1 μm grains of crystalline olivine and crystalline enstatite, calculated from n and k from Fabian et al. (2001) and Jäger et al. (1998), respectively.

of the complex index of refraction were determined using Kramers-Kronig relations. Optical constants for hibonite, calculated from reflectance measurements made by Mutschke et al. (2002) covered 2-10,000 μm . Q_{abs} for a Distribution of Hollow Spheres for FeS, SiO_2, and hibonite is shown Figure 3.

3.4. *Phyllosilicates*

Roush et al. (1991) used dispersion analysis to determine the optical constants of saponite over 5-25 μm. Dispersion analysis describes n and k as the summation of the contributions of a set of classical oscillators and relates them via Fresnel's equations. In the Roush et al. (1991) study, a KBr pellet die was used to prepare a pellet of pure saponite, which was pressed with a hydraulic press to produce a highly reflective surface at visible wavelengths. Nonlinear least squares techniques were then used to minimize the differences between the calculated and observed reflectivities (Roush et al. 1991).

Mooney & Knacke (1985) used a combination of reflectance and transmission measurements on mineral thin sections, 50-70 μm thick, to determine the optical constants of

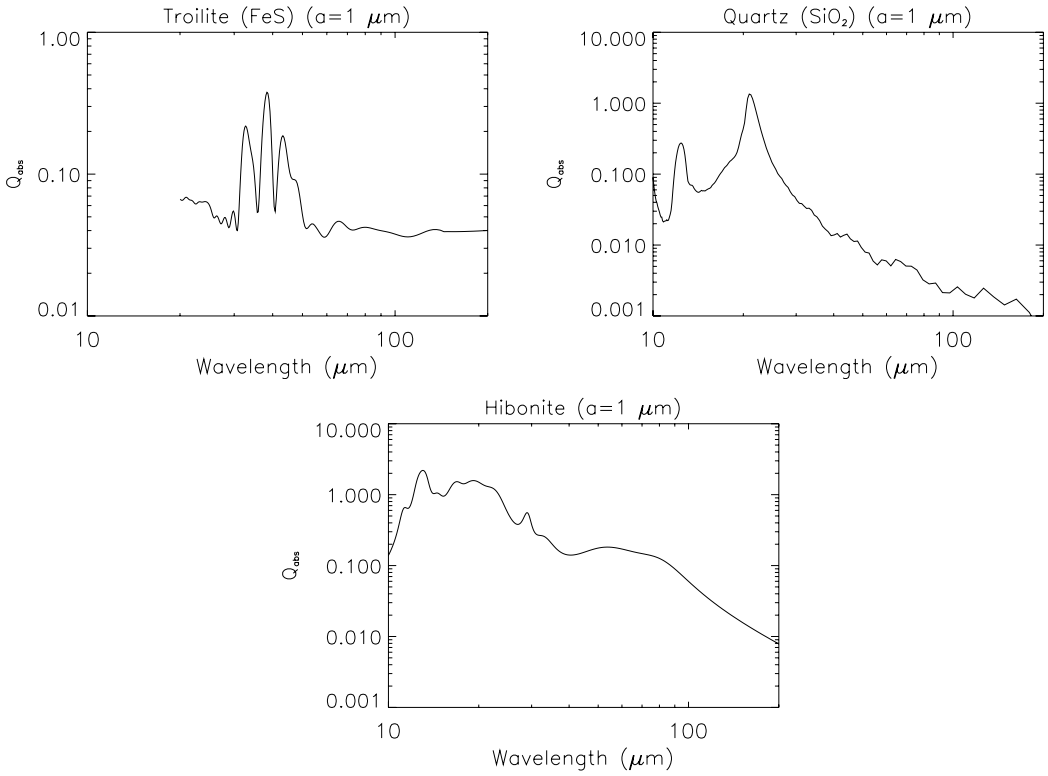

Fig. 3. — Q_{abs} for 1 μm grains of troilite, quartz, and hibonite, calculated from n and k from Begemann et al. (1994), Henning & Mutschke (1997), and Mutschke et al. (2002), respectively.

serpentine and chlorite over 2.5-50 μm. In the region 2.5-5 μm, where transmission is high, Beer's law was applied. For the region > 5 μm, dispersion ananlysis was used (Mooney & Knacke 1985).

The optical constants of montmorillonite were obtained by Toon et al. (1977) over the wavelength range of 5-40 μm. The reader is referred to Toon (1985) for details of the methods used to determine the optical constants.

For the samples provided him, Tim Glotch acquired bidirectional reflectance of specular (or approximately specular) surfaces. He then utilized a classical Lorentz-Lorentz dispersion code that approximates the vibration of the mineral as classical coupled oscillators.

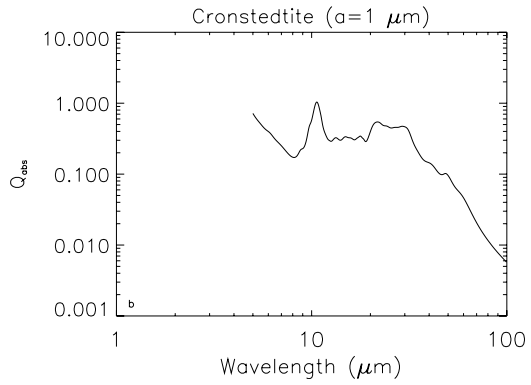

Fig. 4. — Q_{abs} for cronstedtite calculated from n and k determined by Tim Glotch.

The code results in a modeled spectrum, n, and k. An iterative process is used to derive n and k until the modeled spectrum produces a good fit to the measured spectrum. Measurements for all samples were acquired consistently, using the same method, over the same wavelength range (Glotch 2006, personal communication).

Figures 4 and 5 show Q_{abs} for the phyllosilicates of interest to this work. In the case of cronstedtite, no information was available in the literature. Figure 4 shows Q_{abs} for cronstedtite determined by Glotch et al. (2006, in preparation). Figure 5 shows Q_{abs} calculated from the optical constants available in the literature compared to that calculated from the optical constants based on the Glotch (2006) data. It is obvious from the plots that the data from Glotch et al. (2006, in preparation) is at much higher resolution and covers a larger wavelength range.

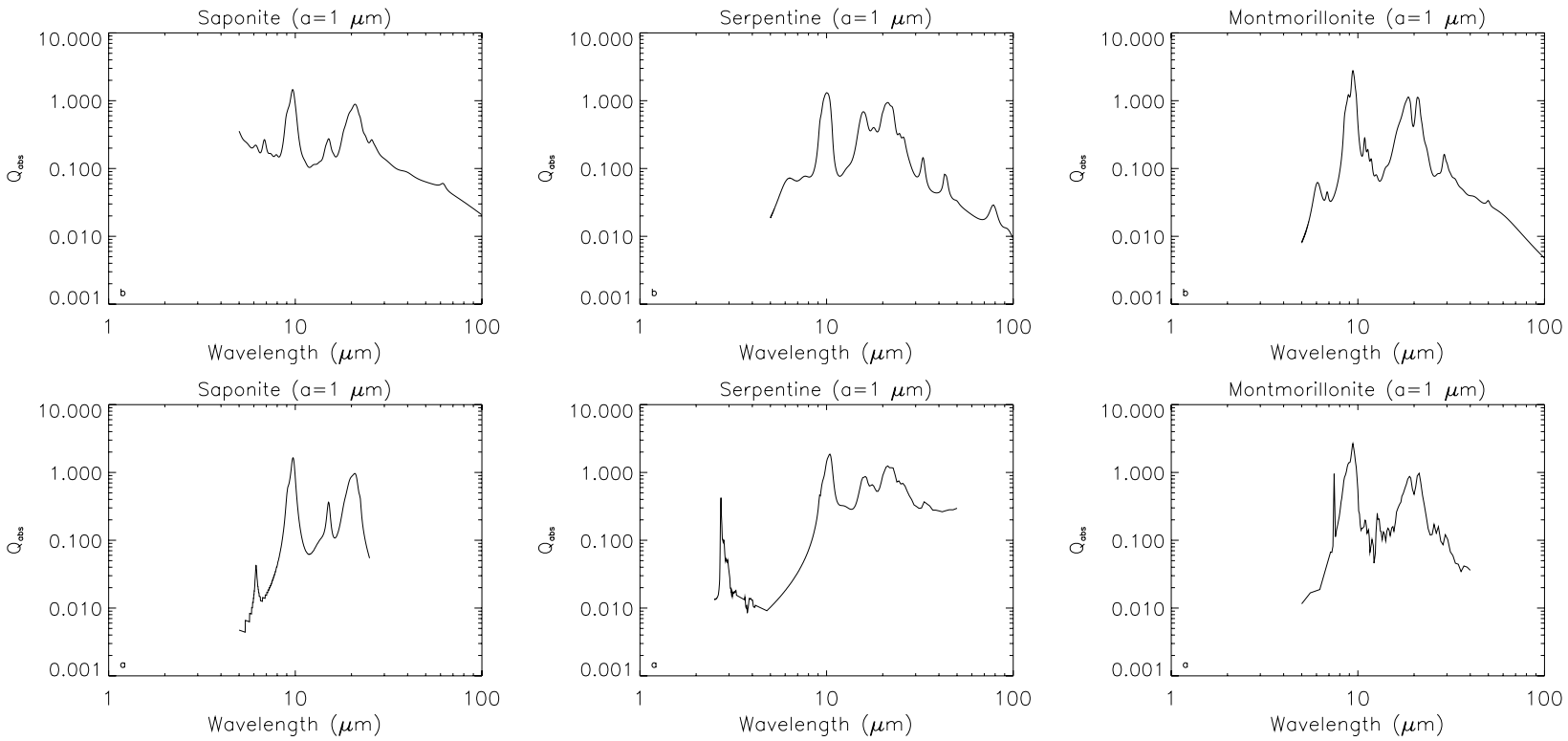

Fig. 5. — *Top Row)* Q_{abs} for saponite, serpentine, and montmorillonite calculated from n and k determined by Tim Glotch. *Bottom Row* Q_{abs} for 1 μm grains of saponite, serpentine, and montmorillonite, calculated from n and k from Roush et al. (1991), Mooney & Knacke (1985), and Toon et al. (1977), respectively.

CHAPTER 3

RADIATIVE TRANSFER MODEL

The development of a model that produces a spectral energy distribution (SED) for comparison to observations requires an understanding of the theory of radiative transfer. In this work, radiative transfer will be used to describe how electromagnetic radiation emitted from the central star is absorbed and reemitted by the surrounding disk.

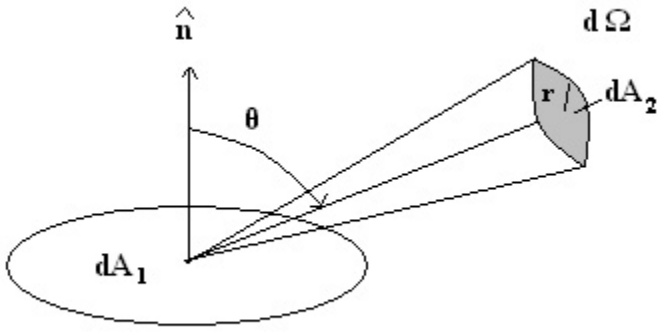

Fig. 6. — Flux geometry

1. Radiative Transfer Primer

A spherically symmetric, isolated star is an example of an isotropic radiation source, where energy is emitted equally in all directions. The flux from such a source is a measure of the amount of energy passing through a given area (Figure 6). The energy crossing an area dA_1, into a solid angle $d\Omega$, in time dt, and frequency range $d\nu$ is given by (Rybicki & Lightman 1979).

$$dE_\nu = I_\nu \, dA \, dt \, d\Omega \, d\nu, \tag{3.1}$$

where I_ν is the specific intensity and the solid angle, $\mathrm{d}\Omega$, is defined as

$$d\Omega = \frac{dA_2}{r^2}.$$

For a sphere,

$$d\Omega = \frac{4\pi r^2}{r^2} = 4\pi \text{ sr (steradian)}.$$

Assuming axisymmetry (i.e. slab geometry) and integrating over all solid angles we have

$$\int_{4\pi} d\Omega = 2\pi \int_{-1}^{1} d\mu,$$

where $\mu = \cos\theta$.

The emergent flux from an isotropically emitting blackbody is (Rybicki & Lightman 1979)

$$F = \pi \int_{\nu} B_\nu d\nu = \pi B(T) = \sigma T^4, \tag{3.2}$$

where σ is the Stefan-Boltzmann constant (5.67 x 10^{-5} erg cm^{-2} K^{-4} s^{-1}) and B_ν is the Planck function. Expressed per unit frequency, the Planck function is

$$B_\nu(T) = \frac{2h\nu^3/c^2}{e^{h\nu/kT} - 1}. \tag{3.3}$$

If the Planck function is expressed per unit wavelength, rather than per unit frequency it becomes

$$B_\lambda(T) = \frac{2hc^2/\lambda^5}{e^{hc/\lambda kT} - 1}. \tag{3.4}$$

If radiation passes through matter (such as dust), absorption, emission, and scattering can occur, resulting in a change in the specific intensity. For absorption only, the specific intensity is given by

$$I_\nu = I_\nu(0)e^{-\tau_\nu}, \tag{3.5}$$

where $I_\nu(0)$ is the initial specific intensity from the source and τ_ν is the *optical depth*. The optical depth is essentially a measure of transparency, giving the fraction of radiation that is absorbed or scattered as it passes through a medium. For example, a medium that is completely transparent has an optical depth of zero (Carroll & Ostlie 1996). The optical depth along a line of sight, ds, is given by

$$\tau_\nu = -\kappa_\nu \rho \, ds, \tag{3.6}$$

where κ is the opacity (units cm^2/g), and ρ is the density of the material (Carroll & Ostlie 1996). The change in specific intensity of a ray passing through an infinitesimal optical depth, is given by (Rybicki & Lightman 1979)

$$dI_\nu = -I_\nu \, d\tau, \tag{3.7}$$

which gives

$$\frac{dI_\nu}{d\tau_\nu} = -I_\nu. \tag{3.8}$$

Rewriting τ_ν per equation 3.6, and adding emission gives (Rybicki & Lightman 1979; Carroll & Ostlie 1996)

$$dI_\nu = -\kappa_\nu \rho I_\nu \, ds + j_\nu \rho \, ds, \tag{3.9}$$

where j_ν is the emission coefficient. Dividing both sides by $-\kappa_\nu \rho \, ds$ gives

$$-\frac{1}{\kappa_\nu \rho}\frac{dI_\nu}{ds} = I_\nu - \frac{j_\nu}{\kappa_\nu}, \tag{3.10}$$

which yields

$$\frac{dI_\nu}{d\tau_\nu} = -I_\nu + S_\nu, \tag{3.11}$$

where S_ν is the *source function*, which describes how photons are removed and replaced by the surrounding medium (Carroll & Ostlie 1996). The solution to this differential equation, under the assumption of uniform S_ν, gives the complete equation of radiative transfer:

$$I_\nu(\tau_\nu) = I_\nu(0) \, e^{-\tau_\nu} + S_\nu(1 - e^{-\tau_\nu}). \tag{3.12}$$

1.1. *Optically Thick Limit*

In the limit of large optical depth, where $\tau_\nu \gg 1$, the radiation field comes into thermal equilibrium with the surrounding medium. In this case, $e^{-\tau_\nu}$ in equation 3.12 goes to zero, which gives

$$I_\nu(\tau_\nu) = S_\nu. \tag{3.13}$$

For thermal radiation, the source function is equal to the Planck function, B_ν, so in the optically thick limit

$$I_\nu(\tau_\nu) = B_\nu(T), \tag{3.14}$$

where T is the temperature of the optically thick medium. In other words, in the limit of large optical depth, the radiation will resemble radiation from a blackbody.

1.2. *Optically Thin Limit*

In the optically thin limit, $\tau_\nu \ll 1$. In this case, $e^{-\tau_\nu} \rightarrow (1 - \tau_\nu)$, which gives (from equation 3.12)

$$I_\nu(\tau_\nu) = \tau_\nu S_\nu + I_0(1 - \tau_\nu). \tag{3.15}$$

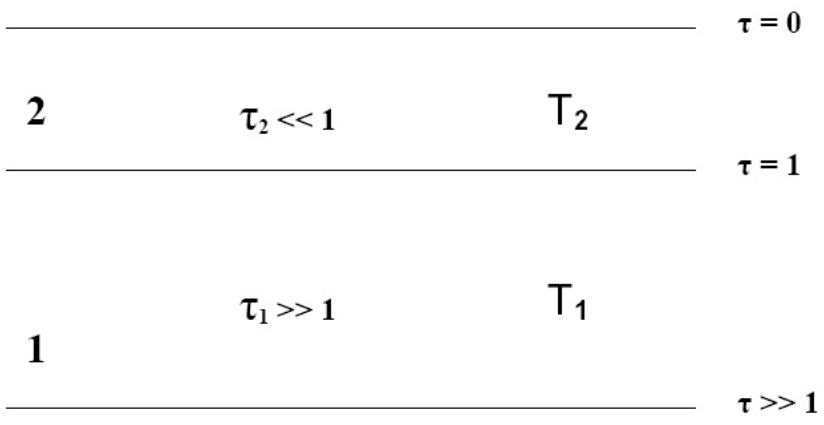

Fig. 7. — An optically thin slab over an optically thick slab

In the case of local thermodynamic equilibrium (LTE), $S_\nu = B_\nu$, even if $I_\nu \neq B_\nu$. The assumption of LTE simply means that although the temperature, pressure, and chemical potential of the disk as a whole may vary globally, these properties are varying so slowly for any one point in the disk that one can assume thermodynamic equilibrium in the immediate area about that point. In the simplest case, where $I_0 = 0$, $I_\nu = \tau_\nu S_\nu$. Rewriting τ_ν as $\rho\kappa_\nu L$, the specific intensity of an optically thin slab of thickness, L, is therefore

$$I_\nu(\tau_\nu) = \rho\kappa_\nu L\, B_\nu(T), \tag{3.16}$$

where T is the temperature of the optically thin medium.

1.3. *Optically Thin Layer over Optically Thick Layer*

Now consider an optically thin surface layer on top of an optically thick interior, as depicted in Figure 7. The emission from the optically thick layer (area 1 of Figure 6),

according to Section 1.1 is

$$I_{\nu_1}(\tau_{\nu_1}) = S_{\nu_1} = B_{\nu_1}(T_1). \tag{3.17}$$

For the optically thin layer, I_0 is no longer zero, but is the emission from the optically thick layer, which yields

$$\begin{aligned} I_{\nu_2}(\tau_{\nu_2}) &= \tau_{\nu_2} B_{\nu_2}(T_2) + I_{\nu_1}(\tau_{\nu_1})(1 - \tau_{\nu_2}) \\ &= B_{\nu_1}(\tau_{\nu_1}) + \rho\kappa_{\nu_2} L_2 \left[B_{\nu_2}(T_2) - B_{\nu_1}(T_1)\right]. \end{aligned} \tag{3.18}$$

In all cases, if T is increased, the flux (B_ν) is increased. Therefore, if $T_2 > T_1$, the quantity in square brackets is a positive number. As a result, an increase in the thickness of the optically thin layer, L_2, or in the opacity, κ_{ν_2}, will result in an increase in emission from the layer. At frequencies where κ_{ν_2} is at a peak, an emission feature results. At any rate, if the temperature is known, the emitted flux can be determined.

1.4. *Radiative Equilibrium*

In this study, only those cases where the material is in radiative equilibrium are considered. In radiative equilibrium, the radiation emitted, for example from a particle of dust, is equal to the radiation absorbed. The emission, over all frequencies, is given by

$$4\pi a^2 \int_\nu Q_{abs_\nu} \pi B_\nu(T)\, d\nu, \tag{3.19}$$

and the absorption, over all frequencies, is given by

$$4\pi a^2 \int_\nu Q_{abs_\nu} \pi J_\nu \, d\nu, \tag{3.20}$$

where a is the particle size, and J_ν is the mean intensity, defined by

$$J_\nu = \frac{1}{4\pi} \int_{4\pi} I_\nu \, d\Omega. \tag{3.21}$$

Equating the emission and absorption gives

$$\int_\nu Q_{abs_\nu} \, B_\nu(T) \, d\nu = \int_\nu Q_{abs_\nu} \, J_\nu \, d\nu. \tag{3.22}$$

This tells us that under conditions of radiative equilibrium, the temperature of a particle can be determined, given the particle emissivity, Q_{abs_ν}, and the mean intensity, J_ν.

2. Applications

The theory of radiative transfer, as described above in simplified form, has several applications of interest to this study. For debris disks and the zodiacal dust of the Solar System, in which case the medium is optically thin, calculation of the modeled SED is fairly straightforward, and a rough estimate can be easily obtained. The modeling of the SED for protoplanetary disks is much more complicated and will be addressed in Section 3.

2.1. *Debris Disks*

Debris disks are circumstellar disks of dust surrounding many mature stars. They are distinct from protoplanetary disks in that the accretion disk of gas and dust from which any planetesimals and/or planets may have formed has dissipated. Debris disks are believed to be the result of collisions of planetesimals and the sublimation of comets, as the dust in circumstellar disks would dissipate in $< 10^4$ years due to a combination of radiation pressure from the central star and Poynting-Robertson drag if not for a continuing source of replenishment (Harper et al. 1984). Debris disks contain very little gas, and the dust (typically only $\sim$ one lunar mass) is quite diffuse, therefore optically thin at all wavelengths (Spangler et al. 2001). Because of this, debris disks can easily be approximated as an optically thin slab, using equation equation 3.18.

The average column density of a debris disk, $\bar{\Sigma}_{dd}$, can be approximated as $M_{dd}/\pi R_{dd}^2$, where M_{dd} is the mass of the disk and R_{dd} is the radius of the disk. Debris disk masses generally are on the order of 0.01 - 10 $M_\oplus$ (Kenyon & Bromley 2004), with radii at mid-infrared wavelengths on the order of 80 - 350 AU (Holland et al. 1998; Lagrange et al. 2000; Wahhaj et al. 2003; Greaves et al. 2005; Metchev et al. 2005; Su et al. 2005). Using the approximation above, the average column densities of debris disks range from $\sim 10^{-4}$ to $\sim 10^{-7}$ g cm^{-2}, as compared to the column density in the superheated dust layer of a protoplanetary disk, which is on the order of $\sim 10^{-3}$ g cm^{-2}. The radii (at mid-infrared wavelengths), disk masses, and average column densities for a few well-known debris disks are shown in Table 4. Disk masses and radii are from Holland et al. (1998), Lagrange et al. (2000), Wahhaj et al. (2003), Greaves et al. (2005), Metchev et al. (2005), and Su et al. (2005).

Table 4. Representative debris disk column densities

	Disk Mass	Disk Radius	$\bar{\Sigma}_{dd}$ (g cm^{-2})
Vega	3 x 10^{-3} $M_\oplus$	330 AU	2.34 x 10^{-7}
β Pic	0.1 $M_\oplus$	80 AU	1.33 x 10^{-4}
Fomalhaut	1.5 lunar masses	80 AU	2.46 x 10^{-5}
AU Mic	0.011 $M_\oplus$	210 AU	2.12 x 10^{-6}
ϵ Eri	0.002 $M_\oplus$	105 AU	1.54 x 10^{-6}

2.2. *Zodiacal Dust*

The zodiacal dust is the main source of mid-infrared sky brightness observed from Earth (Reach et al. 2003). The zodiacal dust is found in a tenuous disk of dust within the inner part of the Solar System. Like debris disks, the zodiacal dust is believed to originate as a result of collisions of planetesimals and the evaporation of comets. Recall that outward radiation pressure and Poynting-Robertson drag would eventually disperse the dust if there were not a source for replenishment (Reach et al. 2003). As in the case of debris disks, emission from the zodiacal dust can be modeled as emission from an optically thin slab.

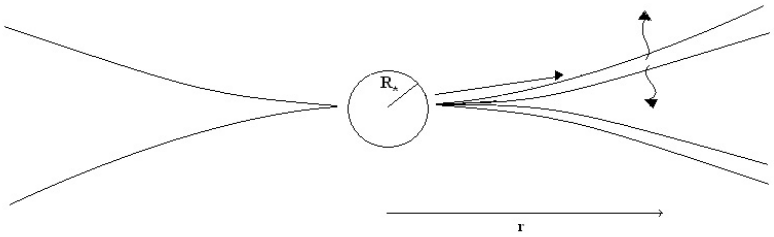

Fig. 8. — A passive, reprocessing disk

3. Protoplanetary Disk Model

Modeling the SEDs of protoplanetary disks, which are typically $\sim$ 0.01 - 0.1 $M_{\odot}$ of gas and dust, is a much more complicated matter than modeling the SEDs of debris disks or the zodiacal dust because they are optically thick. The model presented in this study is based on the model of Chiang & Goldreich (1997). They present a model of a passive, flared disk in hydrostatic and radiative equilibrium. A passive disk has no intrinsic luminosity, but simply reradiates the energy it has absorbed from the central star. The disk is comprised of an optically thin layer of superheated dust grains encasing an optically thick interior. This superheated dust layer emits one-half of the absorbed stellar energy to space and the other half to the interior, thus regulating the temperature of the disk (Figure 8).

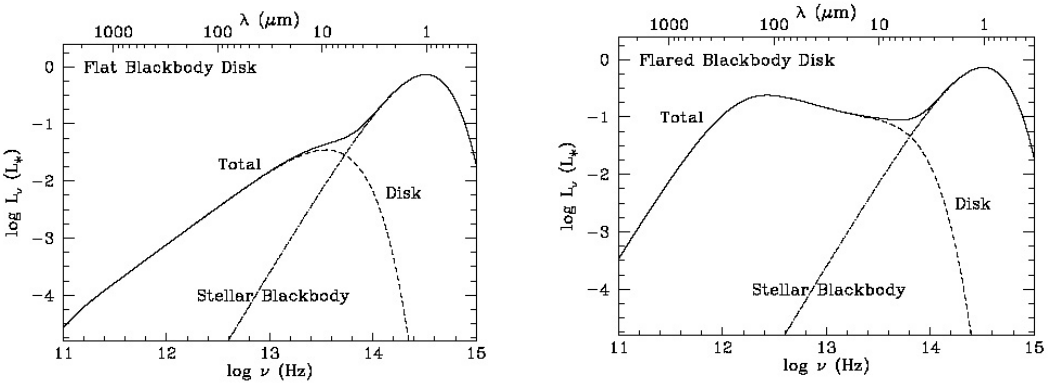

Fig. 9. — Modeled SEDs of a flat, blackbody disk and a flared, blackbody disk from Chiang & Goldreich (1997). Note the flattish spectrum of the flared disk (from 1 - 300 μm) compared to the much steeper spectra of the flat disk. This results because flared disks capture and reprocess more stellar radiation, although typically at lower T and larger λ.

3.1. *Pysical Basis for the Model*

Standard models of a flat, blackbody disk yield an SED in the form of $\nu F_\nu \propto \nu^n$ with $n = \frac{4}{3}$, as do actively accreting disks with uniform rates of mass accretion. However, observations show that most sources have a flattish spectra, with $n \leq \frac{3}{4}$. This discrepancy led to the development by Kenyon & Hartmann (1987) of the flared disk model. In the Kenyon & Hartmann model, the disk flares with increasing radius as a result of vertical hydrostatic equilibrium, thereby intercepting more stellar radiation than the standard flat model. The flared, reprossessing disk model reproduces the observed flat spectra, as shown in Figure 9.

Assuming isothermal conditions, vertical hydrostatic equilibrium results in a flared disk because

$$h = \frac{c_s}{\Omega} \tag{3.23}$$

increases with r more steeply than r^1. Here, h is the scale height (the vertical distance over which the density decreases by a factor of e), c_s is the sound speed and Ω is the Keplerian orbital frequency. As a function of radius, c_s goes as $r^{-3/8}$, assuming $T \propto r^{-3/4}$, and Ω goes as $r^{-3/2}$. Although both decrease with radius, Ω falls off more rapidly, leading to an increase in scale height with radius. Because the height of the visible "photosphere", $H \approx 4h$, increases with radius faster than the radius, the surface intercepts some stellar radiation at all radii (Dullemond 2002). If the size of the dust grains in the surface layer is less than the wavelength of radiation absorbed, $Q_{abs_\nu} < 1$, and the grains are heated to a higher temperature (typically three times that of a blackbody), resulting in a superheated

dust layer, in which they are exposed directly to starlight, as opposed to radiation from neighboring grains (Chiang 2004).

3.2. *Model Assumptions*

The Chiang & Goldreich (1997) model assumed a T Tauri star with a passive, reprocessing disk (Figure 10). The star was modeled as a spherical blackbody with a temperature, $T_* = 4000$ K, mass, $M_* = 0.5\ M_\odot$, and radius, $R_* = 2.5\ R_\odot$. The surface mass density used is approximately that of the minimum-mass solar nebula, $\Sigma = r_{AU}^{-3/2}\ \Sigma_0$ where r_{AU} is the disk radius in astronomical units and $\Sigma_{1AU} = 10^3$g cm^{-2}. The dust and the gas in the disk are uniformly mixed, with dust comprising 1% of the total mass, yet dominating the continuum opacity. The dust is modeled as spherical grains with radius, $a = 0.1\ \mu$m and density of $\rho_d = 2$ g cm^{-3}. For wavelengths at which $\lambda \leq 2\pi a$, the emissivity, $\epsilon = 1$. For the case $\lambda \geq 2\pi a$, $\epsilon = 2\pi a/\lambda$, and decreases with λ. Chiang & Goldreich (1997) made the approximation $\epsilon \approx 8\pi akT/hc \approx T/T_*$, where T is the temperature of the dust. The opacity at visual wavelengths is assumed to be $\kappa = 400$ cm^2 g^{-1}, which gives an optical depth vertically through the disk, at visual wavelengths, of $\tau_V = 4$ x $10^5\ r_{AU}^{-3/2}$ (Chiang & Goldreich (1997).

Chiang & Goldreich (1997) chose an inner radius of $r_i \approx 6R_* \approx 0.07$ AU to coincide with the condensation boundary of most silicates. (Alternatively, Chiang et al. (2001) chose an inner radius, $r_i = 2R_*$, as this is the distance where iron is at its sublimation temperature near T Tauri stars). An outer radius, $r_o \approx 2.3$ x $10^4\ R_* \approx 2.7$ x 10^2 AU was chosen to accomodate the largest disks in the Orion Nebula. All SEDs were computed for disks viewed face-on (Chiang & Goldreich 1997).

The grazing angle, α, is given by

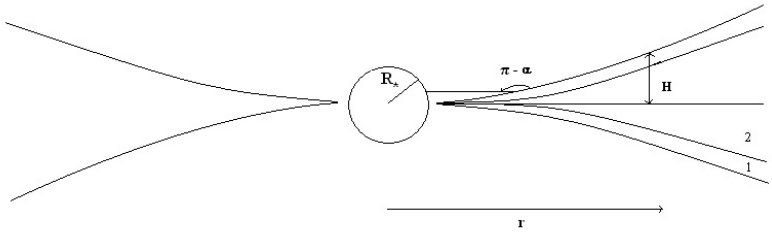

Fig. 10. — Passive, reprocessing disk, where α is the grazing angle, H is the height of the visible photosphere, area 1 is the superheated dust layer, and area 2 is the disk interior.

$$\alpha = \frac{dH}{dr} - \frac{H}{r} = r\frac{d}{dr}\left(\frac{H}{r}\right). \tag{3.24}$$

In the limit of a very thin, or flat disk (basically any disk sufficiently close to the star), $\alpha = 0.4R_*/r$, giving, in general,

$$\alpha \approx \frac{0.4R_*}{r} + r\frac{d}{dr}\left(\frac{H}{r}\right). \tag{3.25}$$

Assuming the gas in the disk is vertically isothermal, the force equation gives a Gaussian vertical density profile

$$\frac{\rho(z)}{\rho(0)} = \exp\left(\frac{-z^2}{2h^2}\right). \tag{3.26}$$

Chiang & Goldreich (1997) give the effective temperature of the disk as

$$T_e = \left(\frac{\alpha}{2}\right)^{1/4}\left(\frac{R_*}{r}\right)^{1/2} T_*. \tag{3.27}$$

However, balancing the absorbed and the emitted flux of the disk gives

$$T_e = \alpha^{1/4} \left(\frac{R_*}{r} \right)^{1/2} T_*, \tag{3.28}$$

a difference of a factor of $2^{1/4}$. Using equations 3.25 and 3.28 we can solve for $H/r \approx 4h/r$

$$\frac{H}{r} \approx 4 \left(\frac{T_*}{T_c} \right)^{4/7} \left(\frac{r}{R_*} \right)^{2/7}, \tag{3.29}$$

where

$$T_c \equiv \frac{GM_* \mu_g}{kR_*}.$$

Here, k is Boltzmann's constant and μ_g is the mean molecular weight of the gas. Balancing emission and absorption of the dust in the outer surface layer gives an approximation of the temperature of the superheated dust

$$T_{ds} \approx \frac{1}{\epsilon_s^{1/4}} \left(\frac{R_*}{2r} \right)^{1/2} T_*. \tag{3.30}$$

Since the superheated dust layer emits one-half of its radiation to the disk interior, the interior disk temperature is given by

$$T_i \approx \left(\frac{\alpha}{2} \right)^{1/4} \left(\frac{R_*}{r} \right)^{1/2} T_*. \tag{3.31}$$

This is the temperature at which all the inward-directed radiation is thermalized, in the region where the disk is opaque to blackbody radiation. In addition, Chiang & Goldreich (1997) give the temperature at further radii, where the disk is optically thin to its own radiation, but still opaque to radiation from the superheated dust layer. They also derive the temperature at still further radii, where the disk is transparent to both its own radiation and that from the surface layer. These latter two temperatures only apply at radii greater than 80 - 100 AU, and can reasonably be ignored for the purposes of this study, which focuses on emission at 10 μm and 20 μm, and therefore, $T \geq 100$ K and $r <$ tens of AU.

3.3. *Improvements to the Chiang & Goldreich Model*

For this study, the model of Chiang & Goldreich (1997) was followed, with a few changes and improvements. As noted previously, the effective temperature of the disk as derived by Chiang & Goldreich (1997), and consequently the interior temperature of the disk, was off by a factor of $2^{1/4}$. More importantly, actual dust opacities were calculated utilizing optical constants obtained experimentally by Timothy Glotch (in the case of phyllosilicates) or those published in the literature. Finally, rather than modeling the central star as a simple blackbody, the 1993 Kurucz models of stellar atmospheres were used (Kurucz 1993).

The parameters of the model include a T Tauri star of effective temperature, $T_* = 6000$ K, mass, $M_* = 1\ M_\odot$, and radius, $R_* = 1\ R_\odot$, with a passive, flared, reprocessing disk. The distance to the star is 145 parsecs (approximately the distance to the Upper Scorpius star-forming region). The inner radius of the disk is located 2 AU from the central star, and the outer radius of the disk was set at 80 AU. The self-consistent grazing

angle was calculated per Equation 3.24. The stellar spectrum was determined using the 1993 Kurucz model for a star with a surface temperature of 6000 K. The total opacity was then computed using a Distribution of Hollow Spheres and a population of grains of different compositions. This done, the surface density, Σ_0, yielding an optical depth at visual wavelengths equal to unity ($\tau_V = 1$) was determined. Calculation of the Planck-averaged total opacity at visual wavelengths gives the value for Σ_{ds}, the surface density of the superheated dust layer.

Once opacities were known, the temperature of the dust in the superheated layer of the disk could be determined. As optical constants were not available at visual wavelengths, the assumption was made that all the superheated dust was at the same temperature as amorphous forsterite, which is assumed to dominate the opacity. This is a good approximation if the dust is thermally coupled, although admittedly it probably is not. The knowledge of the temperature of the superheated dust layer allows for the calculation of the contribution of this layer to the overall SED and was used to calculate the temperature of the interior of the disk. Once the temperature of the interior was known, its contribution to the SED was determined. Then the spectral emissions from the star, the superheated dust layer, and the disk interior were combined, resulting in the modeled SED (Figure 11).

A combination of grain compositions was used based upon the minerals expected to be present in disks, as outlined in Chapter 2. Overall composition of the dust included mainly amorphous forsterite and enstatite, with small amounts of crystalline olivine, crystalline enstatite, FeS (troilite), quartz, and hibonite. The relative percentages of each mineral in each case are shown in Table 5.

Opacities were calculated based upon a grain size of 0.1 μm . The effect of phyllosilicates on the spectra was tested by replacing 3% of the amorphous forsterite with an equal

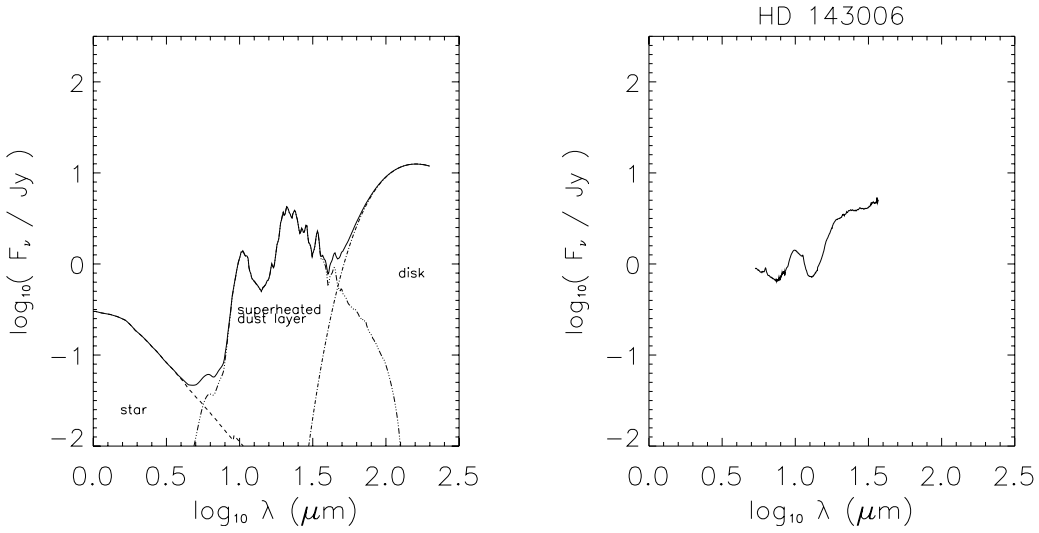

Fig. 11. — (Left) Modeled SED of a passive, flared, radiative equilibrium disk, showing contributions from the star, the disk, and the superheated dust layer. (Right) SED of HD 143006, as measured by the Spitzer Space Telescope, is shown for comparison.

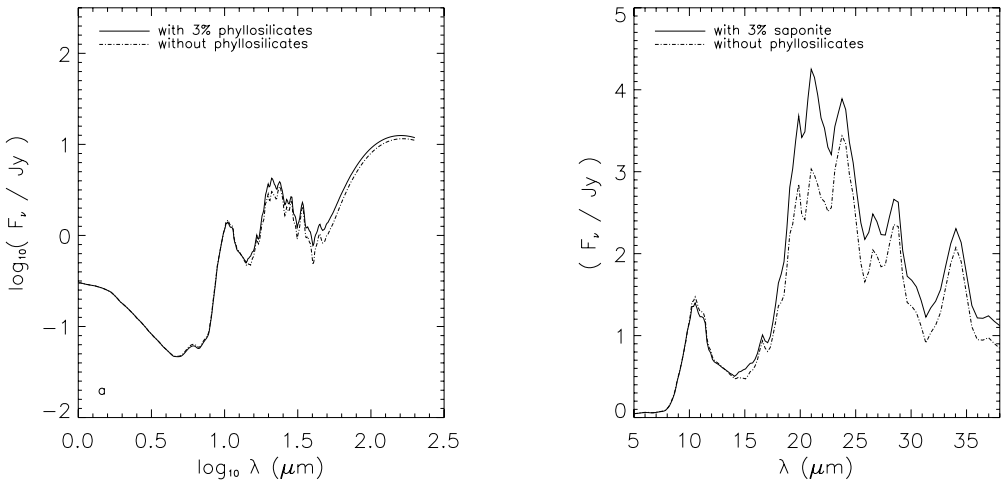

Fig. 12. — **a)** Modeled SED with and without the inclusion of 3% phyllosilicates. **(**b) Close-up view of the area of the SED where the contribution from the superheated dust layer dominates.

Table 5. Relative percentages of the minerals used in modeled SEDs.

	Mineral Percentages	
	Without Phyllosilicates	With Phyllosilicates
amorphous forsterite	58	55
amorphous enstatite	32	32
crystalline olivine	3	3
crystalline enstatite	2	2
FeS (troilite)	2	2
quartz	2	2
hibonite	1	1
saponite	0	3

amount of saponite (the most common phyllosilicate found in the matrix of meteorites). The value of 3% was chosen in that 20% phyllosilicates in the inner 2-4 AU of the disk (consistent with the Reach et al. (2003) model of the zodiacal dust) results in a phyllosilicate content overall of 3%.

3.4. *Results*

The difference in the SED resulting from the inclusion of 3% phyllosilicates is dramatically evident, as shown in Figures 12 and 13,. The effect of the inclusion of saponite can easily be observed at $\sim$ 9 μm , 10-11 μm , 15 μm , 26 μm , 29-31 μm , and especially at $\sim$ 21 μm (Figure 12). To insure that the difference observed was due to the inclusion of phyllosilicates, rather than the decrease in the amount of amorphous forsterite, modeled SEDs were produced with 75% amorphous forsterite and 12% amorphous enstatite in one case and 12% amorphous forsterite and 75% amorphous enstatite in another (with all other relative percentages remaining the same as in Table 5). The difference between the SEDs with and without the inclusion of 3% phyllosiicates is still evident, as shown in Figure 14.

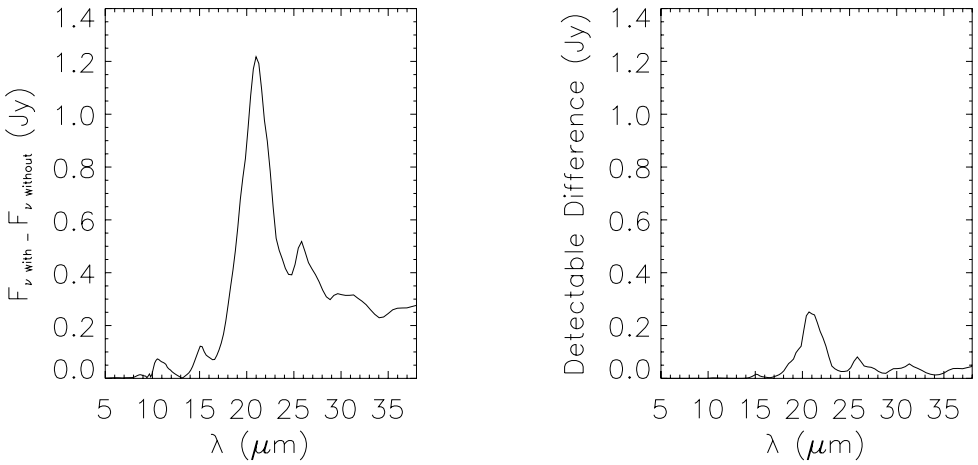

Fig. 13. — (Left) Difference between the modeled spectrum with and without 3% phyllosilicates (saponite). (Right) Detectable difference between the modeled spectrum with and without 3% phyllosilicates after accounting for noise.

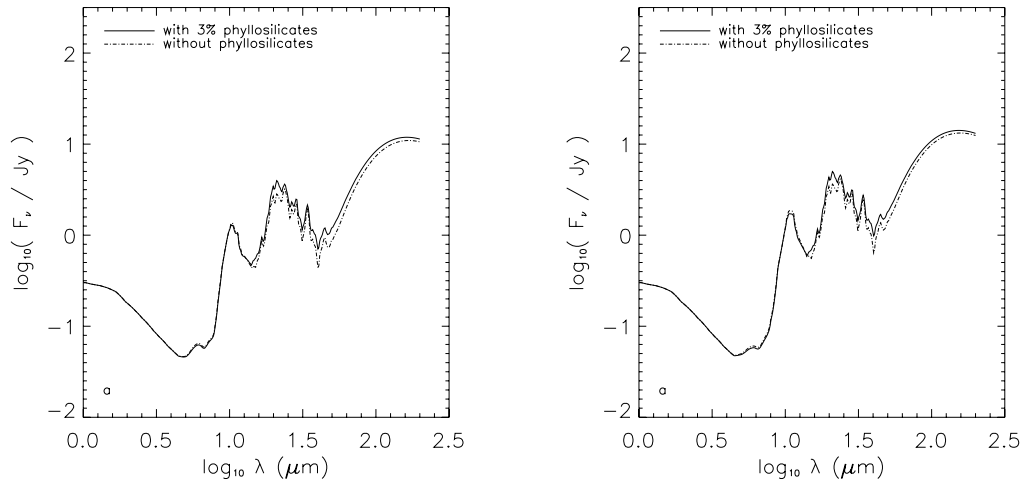

Fig. 14. — (Left) Difference between the modeled spectrum with and without 3% phyllosilicates (saponite). All relative percentages are the same as in Table 5, other than amorphous forsterite at 75% and amorphous enstatite at 12%. (Right) Difference between the modeled spectrum with and without 3% phyllosilicates (saponite). All relative percentages are the same as in Table 5, other than amorphous forsterite at 12% and amorphous enstatite at 75%.

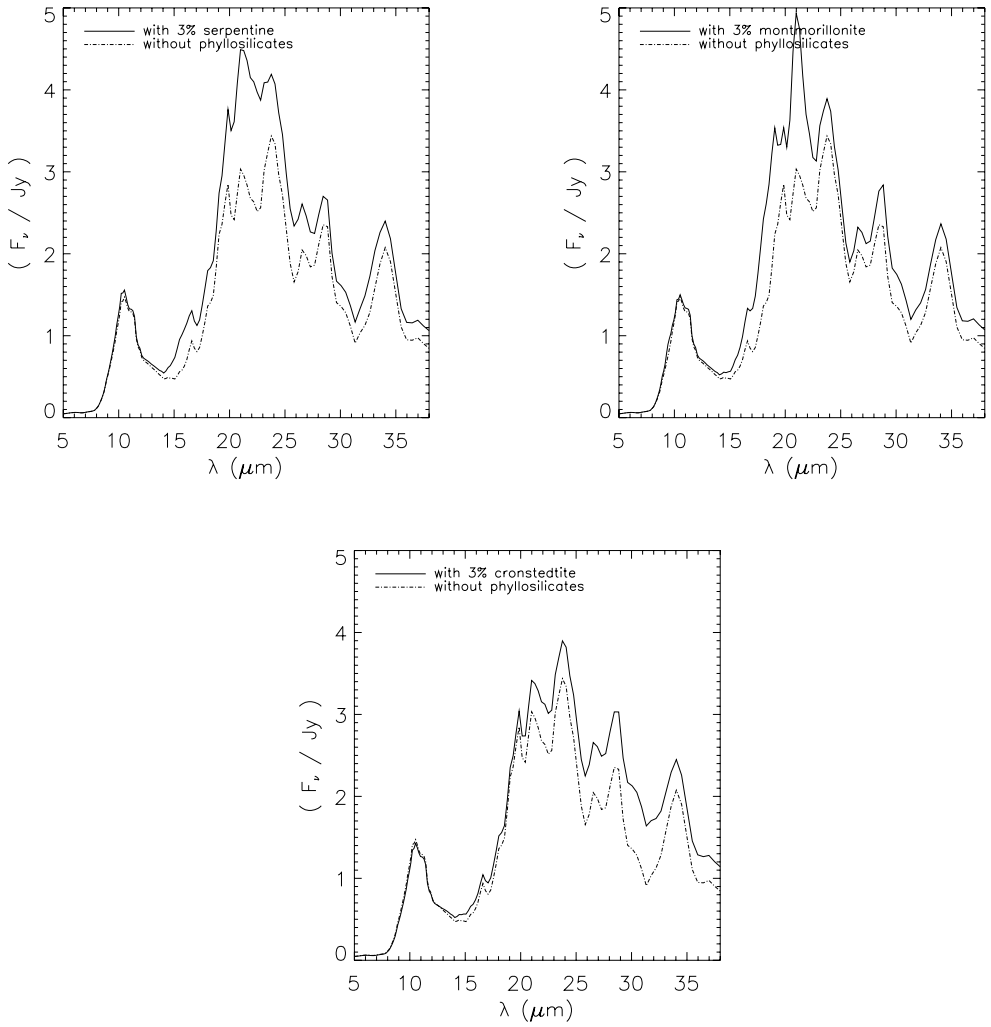

Fig. 15. — Difference between the modeled spectrum with and without 3% serpentine, montmorillonite, or cronstedtite.

Inspection of Figure 12 shows that the overall flux is increased with the inclusion of phyllosilicates, with the major spectral features located at the same wavelength as without phyllosilicates. At first glance, it would seem that it would be difficult to distinguish between an SED with or without phyllosilicates. While there are significant differences in the calculated models with and without phyllosilicates, broad differences in level can be difficult to detect in the spectra of astrophysical objects due to uncertainties in the exact shape of the underlying continuum and foreground extinction and screening. In practical settings, detection is both easier and more reliable if it involves comparison of distinct features that can be isolated from the background. Upon closer examination, one notes higher emission at ~ 21 μm than ~ 24 μm in the SED including phyllosilicates. In the SED without phyllosilicates, however, the reverse is true; the ~ 24 μm emission is greater than the ~ 21 μm emission. These two features allow one to approach the question of detectability in a more meaningful way than simply measuring the difference in flux resulting from the inclusion of phyllosilicates. As the modeled SED shown in Figure 12 is representative of the inclusion of saponite, it was necessary to determine if the same trend was seen when including different species of phyllosilicates. Modeled SEDs with the inclusion of 3% serpentine, montmorillonite, or cronstedtite are shown in Figure 15. From the figure, it appears that this ratio may turn out to be diagnostic of serpentine and montmorillonite, but is not diagnostic of the presence of cronstedtite.

3.5. *Possibility for Detection*

The question remains whether the detection of the effects of phyllosilicates on the 21 μm /24 μm ratio is possible with the instruments reviewed earlier in this work. To make this determination, it is first necessary to examine how noise will affect the SED.

It is important to remember that the shot-noise in a signal, or photon-noise (the noise assoicated with the signal itself), follows a Poisson distribution, for which the standard deviation equals the square root of the measured quantity. In this case, this means that the shot-noise is proportional to the square root of the signal received. This tells us that uncorrelated errors in a signal add quadratically.

The noise present in the measured flux, F_λ, without the inclusion of phyllosilicates is given by

$$\sigma^2_{F_\lambda} = NIt + NSt + NDt + N\sigma^2_R, \tag{3.32}$$

where N is the number of pixels on which the signal is recorded, S is the background noise from the sky (in electrons/pixel/second; the conversion from true brightness, in ergs cm^{-2} s^{-1} μm $^{-1}$, involves the aperature and sensitivity of the instrument used to measure the signal), D is the dark current, t is the integration time, σ_R is the read noise, and I is the intensity of the signal (in electrons/pixel) at a given wavelength. The noise in the flux measured after the inclusion of phyllosilicates is

$$\sigma^2_{F_\lambda+\Delta F_\lambda} = N(I + I\delta)t + NSt + NDt + N\sigma^2_R, \tag{3.33}$$

where $\delta = \Delta F_\lambda / F_\lambda$. Recalling that noise adds in quadrature, this gives the total noise in the difference as

$$\begin{aligned}\sigma^2_{\Delta F_\lambda} &= \sigma^2_{F_\lambda} + \sigma^2_{F_\lambda + \Delta F_\lambda} \\ &= 2NIt + 2NSt + 2NDt + 2N\sigma^2_R + NI\delta t. \end{aligned} \tag{3.34}$$

Absorbing the dark current into the background noise, the wavelength-dependent signal-to-noise in the difference, Σ_Δ, is then given by

$$\Sigma_\Delta = \frac{N(I\delta)t}{\sqrt{(N)}\left[2(I+S)t + 2\sigma^2_R + \delta It\right]^{1/2}}. \tag{3.35}$$

Detectability threshholds for instruments are given in terms of the time, t_0 needed to detect a signal of strength I_0 with signal-to-noise, Σ_0.

$$\Sigma_0 = \frac{N_0 I_0 t_0}{\sqrt{(N_0)}\left[I_0 t_0 + S_0 t_0 + \sigma^2_R\right]^{1/2}}. \tag{3.36}$$

It is now possible to calculate what integration time is necessary in 3.35 to achieve the threshold S/N, Σ_0, of a number of the instruments discussed in Chapter 1.

The spectral resolution, $R = \lambda/\Delta\lambda$, required for detection of the features at ~ 21 and 24 μm is determined by measuring the full width at half maximum (FWHM) of the feature at the given wavelength. The value of R_0 is given by the spectral resolution reported on each instrument as detailed in Chapter 1 of this work. The number of pixels over which the signal is recorded must also be taken into account when determining spectral resolution. This results in the relationship $N/N_0 = R_0/R$, where $N = \Delta\lambda_R/\text{pixels}$, $N_0 = \Delta\lambda_{R_0}/\text{pixels}$. Using this relationship gives $N = N_0\frac{R_0}{R}$. As $I/I_0 = F_\lambda/F_0$, $I = \frac{F_\lambda}{F_0}I_0$, where F_0 is the

flux measured at the given wavelength by the instrument (the sensitivity). Making the substition, $t = \tau\ t_0$ gives

$$\Sigma_\Delta = \frac{\frac{F_\lambda}{F_0} I_0\ \delta\ \tau\ t_0\ \frac{R_0}{R}\ N_0}{\sqrt{N_0}\sqrt{\frac{R_0}{R}}\left[2\left(\frac{F_\lambda}{F_0} I_0 + S\right)\tau\ t_0 + 2\sigma_R^2 + \delta\left(\frac{F_\lambda}{F_0} I_0\ \tau\ t_0\right)\right]^{1/2}}. \tag{3.37}$$

Making the assumptions that $\sqrt{I} \gg \sigma_R^2$ (shot-noise limited) and $\delta \ll 1$ (the difference in emission due to phyllosilicates is small compared to the total emission without phyllosilicates) gives

$$\Sigma_\Delta = \frac{\frac{F_\lambda}{F_0}\sqrt{\frac{R_0}{R}}\ \delta\ \tau\ I_0\ t_0\sqrt{N_0}}{\sqrt{2\tau}\left[\left(\frac{F_\lambda}{F_0} I_0 + S\right) t_0\right]^{1/2}} = \frac{\frac{F_\lambda}{F_0}\sqrt{\frac{R_0}{R}}\ \delta\ \tau\ I_0\ t_0\ \sqrt{N_0}}{\sqrt{2\tau\ \frac{F_\lambda}{F_0}}\left[\left(I_0 + S\frac{F_0}{F_\lambda}\right) t_0\right]^{1/2}}. \tag{3.38}$$

Now assuming that the source is bright compared to the background ($S \ll I_0$) and that the dark current is negligible ($D \ll I_0$)

$$\Sigma_\Delta = \sqrt{\frac{F_\lambda\ R_0\ \tau}{F_0\ R\ 2}}\ \delta\ \frac{I_0\ t_0\ \sqrt{N_0}}{(I_0\ t_0)^{1/2}} = \sqrt{\frac{F_\lambda\ R_0\ \tau}{F_0\ R\ 2}}\ \delta\ \Sigma_0. \tag{3.39}$$

Recall that $\delta = \Delta F_\lambda / F_\lambda$, which tells us that $\Sigma_\Delta \propto \Delta F_\lambda / \sqrt{2F_\lambda}$, and gives

$$\Sigma_\Delta = \frac{\Delta F_\lambda}{\sqrt{2F_\lambda F_0}}\left(\frac{R_0}{R}\right)^{1/2}\left(\frac{t}{t_0}\right)^{1/2}\ \Sigma_0. \tag{3.40}$$

Let λ_1 = the flux at 21 μm, λ_2 = the flux at 24 μm, and $\mathcal{R} = \frac{F_{\lambda_1}}{F_{\lambda_2}}$. In the modeled SED, $\mathcal{R}$ without phyllosilicates ~ 0.9; with phyllosilicates, $\mathcal{R} \sim 1.2$. If $0.9 < \mathcal{R} < 1.2$, $\Delta\ \mathcal{R} \sim 0.3$. If one wants to measure the value of $\mathcal{R}$ well enough to say at the 10-σ level

that phyllosilicates are present, then $\mathcal{R}$ needs to be measured with a 1-σ uncertainty of 3%. In other words,

$$\left(\sigma \frac{F_{\lambda_1}}{F_{\lambda_2}}\right)^2 = \left(\frac{\sigma F_{\lambda_1}}{F_{\lambda_1}}\right)^2 + \left(\frac{\sigma F_{\lambda_2}}{F_{\lambda_2}}\right)^2 < (0.03)^2 .$$

The signal-to-noise, Σ, at a any given wavelength, i, is given by

$$\Sigma_i = \left(\frac{R_0}{R}\right)^{1/2} \left(\frac{t}{t_0}\right)^{1/2} \left(\frac{F_i}{F_0}\right)^{1/2} \Sigma_0,$$

which yields

$$\frac{1}{\Sigma_1^2} + \frac{1}{\Sigma_2^2} < (0.03)^2 .$$

Now, since $F_{\lambda_1} \sim F_{\lambda_1}$,

$$\frac{2}{\Sigma_{\mathcal{R}}^2} < (0.03)^2 \Rightarrow \Sigma_{\mathcal{R}} > \frac{\sqrt{2}}{0.03}. \tag{3.41}$$

So, for 10-σ detection

$$\left(\frac{R_0}{R}\right)^{1/2} \left(\frac{t}{t_0}\right)^{1/2} \left(\frac{\sqrt{F_{\lambda_1} F_{\lambda_2}}}{F_0}\right)^{1/2} \Sigma_0 \geq \Sigma_{\mathcal{R}}. \tag{3.42}$$

Solving for t gives the minimum instrument-specific integration time necessary to achieve a 10-σ detection

$$t = \left(\frac{\Sigma_{\mathcal{R}}}{\Sigma_0}\right)^2 \left(\frac{F_0}{\sqrt{F_{\lambda_1} F_{\lambda_2}}}\right) \left(\frac{R}{R_0}\right)\ t_0. \tag{3.43}$$

Based upon the modeled SED, $R = 20$, $F_{\lambda_1} = 4250$ mJy, and $F_{\lambda_2} = 3889$ mJy. Table 6 shows t for the Spitzer Space Telescope, SOFIA, Michelle (Gemini North), IRTF, and JWST.

Table 6. Minimum integration times necessary to achieve a 10-σ detection of $\mathcal{R}$.

	t
Spitzer	42 s
SOFIA	115 s
Michelle	1771 s
IRTF	738 s
JWST	1.6 x 10^{-4} s

CHAPTER 4

CONCLUSION AND DISCUSSION

The main focus of this study has been to determine whether phyllosilicates can be detected in extrasolar protoplanetary disks. In the following sections, the possibility of detection and the resulting implications will be discussed based upon the theoretical spectral energy distributions presented in the previous chapter.

1. Is Detection of Phyllosilicates Possible?

In the previous chapter, it was determined, based upon theoretical spectral energy distributions of varying mineralogy, that the detection of 3% phyllosilicates in a protoplanetary disk might be possible by inspection of the 21 μm / 24 μm ratio. The minimum integration times for a 10-σ detection were calculated for five instruments presently in operation or due to be in operation in the near future. In this section, it will be determined whether the minimum integration time calculated is reasonable.

1.1. *Spitzer Space Telescope*

In the implementation of 3.43 for the Spitzer Space Telescope, $T = 1$, $F_0 = 0.4$ mJy at 21 μm, $t_0 = 512$ s, and $R_0 = 60$ at 21 μm. The resulting minimum integration time of 42 s indicates that it is possible to achieve a 10-σ detection with Spitzer.

1.2. *Stratospheric Observatory for Infrared Astronomy (SOFIA)*

For the Echelon-Cross-Echelle Spectrometer (EXES) aboard SOFIA, $T = 4$, $F_0 = 500$ mJy at 21 μm, $t_0 = 900$ s, and $R_0 = 3000$ at 21 μm. The resulting minimum integration time of 115 s (just under two minutes) indicates it is also possible to achieve a 10-σ detection with SOFIA.

1.3. *Michelle*

For Michelle (Gemini North), $T = 5$, $F_0 = 110$ mJy at 21 μm, $t_0 = 3600$ s, and $R_0 = 110$ at 21 μm. The resulting minimum integration time of 1771 s (just under a half-hour) is reasonable provided that the assumptions built into 3.43 are appropriate. For an integration time of this duration, however, they probably are not. Certainly, both the background noise and the dark current will become significant. A closer examination of the noise contributions would be necessary to determine whether it is possible to achieve a 10-σ detection with Michelle.

1.4. *NASA Infrared Telescope (IRTF)*

For IRTF, $T = 1$, $F_0 = 100$ mJy at 21 μm, $t_0 = 60$ s, and $R_0 = 100$ at 21 μm. The resulting integration time of 738 s (just over 12 minutes) is reasonable provided, once again, that the assumptions are correct. For an integration time of 12 minutes, the background and dark current may become meaningful, necessitating a more careful analysis of the noise in order to determine whether it is possible to achieve a 10-σ detection with IRTF.

1.5. *James Webb Space Telescope (JWST)*

For JWST, $T = 10$, $F_0 = 3.9 \times 10^{-4}$ mJy at 21 μm, $t_0 = 10^4$ s, and $R_0 = 3000$ at 21 μm. The resulting minimum integration time of 1.6×10^{-4} s indicates it is possible to achieve a 10-σ detection with JWST.

2. Implications

This study has demonstrated that the most common phyllosilicates found in meteorites should be detectable in protoplanetary disks, at a level of 3%, by examining the ratio of the emission at 21 μm to the emission at 24 μm. The demonstration that phyllosilicates can be detected with the Spitzer Space Telescope is of particular value, considering the availability of large amounts of archived data on protoplanetary and debris disks as a part of the Spitzer Legacy Science Program. In the case of debris disks, the detection may be more difficult, as the overall emission would be considerably less due to the lower column densities.

The implications of detection of phyllosilicates within protoplanetary disks are immense. To date, there has not been such a detection in a protoplanetary disk, so it would represent the identification of a new mineral in such disks. As phyllosilicates are the product of aqueous alteration, detection would represent the first indication of liquid water in an extrasolar system. Needless to say, such a presence of liquid water would have important astrobiological implications. Detection of phyllosilicates in a disk would also demonstrate the system's similarity to our own. A definitive non-detection would place an upper limit on the abundance of phyllosilicates and would indicate that those systems are fundamentally different from the Solar System. However, as this work has demonstrated, phyllosilicates such as cronstedtite could be present in a disk without affecting the ratio of 21 μm to 24 μm emission, presently the only possible diagnostic feature.

Parameter studies are needed to determine the effect of different shape and size distributions (and mineralogy) on the modeled SED. Furthermore, modeled SEDs should be produced for a range of stellar sizes, stellar temperatures, and disk sizes. If these additional

parameter studies consistently show the reversal of the peak emission at 21 μm versus 24 μm with the inclusion of most phyllosilicates, it will clearly demonstrate the usefulness of this ratio as a diagnostic for the presence of phyllosilicates in extrasolar protoplanetary disks.

3. Future Work

Planned work for the future includes obtaining optical constants at visual wavelengths. This will facilitate the calculation of the temperature of each mineral species in the superheated dust layer, eliminating the need to assume that the temperature of all dust in the superheated layer is equal to that of the dominant species. Improved models will be developed that properly treat the transition between the superheated dust layer and the disk interior. Comparisons of these improved models to data available through the Spitzer Legacy Science Program will be performed, including an automated χ^2 fitting routine.

REFERENCES

Adams, F. C., Lada, C. J., & Shu, F. H. 1987, ApJ, 312, 788

Adams, F. C., Shu, F. H., & Lada, C. J. 1988, ApJ, 326, 865

Armstrong, J. T., Meeker, G. P., Huneke, J. C., & Wasserburg, G. J. 1982, Geochim. Cosmochim. Atca, 46, 575

Bischoff, A. 1998, Meteoritics and Planetary Science, 33, 1113

Bischoff, A., & Srinivasan, G. 2003, Meteoritics and Planetary Science, 38, 5

Bohren, C. F., & Huffman, D. R. 1983, *Absorption and Scattering of Light by Small Particles* (New York: Wiley)

Bouwman, J., Meeus, G., de Koter, A., Hony, S., Dominik, C., & Waters, L. B. F. M. 2001, A&A, 375, 950

Bregman, J. D., Witteborn, F. C., Allamandola, L. J., Campins, H., Wooden, D. H., Rank, D. M., Cohen, M., & Tielens, A. G. G. M. 1987, A&A, 187, 616

Browning, L. B., McSween, H. Y., & Zolensky, M. 1994, Lunar and Planetary Institute Conference Abstracts, 25, 181

Buseck, P. R., & Hua, X. 1993, Annual Review of Earth and Planetary Sciences, 21, 255

Calvin, W. M., & King, T. V. V. 1997, Meteoritics and Planetary Science, 32, 693

Carr, M.H., 1996, *Water on Mars* (New York: Oxford University Press)

Carroll, B. W., & Ostlie, D. A. 1996, *An Introduction to Modern Astrophysics* (Reading, MA: Addison-Wesley)

Chiang, E. I., & Goldreich, P. 1997, ApJ, 490, 368

Chiang, E. I., Joung, M. K., Creech-Eakman, M. J., Qi, C., Kessler, J. E., Blake, G. A., & van Dishoeck, E. F. 2001, ApJ, 547, 1077

Chiang, E. I. 2004, ASP Conf. Ser. 309: Astrophysics of Dust, 309, 213

Ciesla, F. J., & Hood, L. L. 2002, Icarus, 158, 281

Ciesla, F. J., Lauretta, D. S., Cohen, B. A., & Hood, L. L. 2003, Science, 299, 549

Clayton, R. N. 1997, Parent-Body and Nebular Modification of Chondritic Materials, 10

"COMICS." May 20, 2006.
URL: http://www.naoj.org/Observing/Instruments/COMICS/index.html

Connolly, H. C., & Love, S. G. 1998, Science, 280, 62

Connolly, H. C., Jr., & Desch, S. J. 2004, Chemie der Erde / Geochemistry, 64, 95

de Pater, I. & Lissauer, J. J. 2001, *Planetary Sciences* (Cambridge: Cambridge University Press)

Desch, S. J., & Connolly, H. C. 2002, Meteoritics and Planetary Science, 37, 183

Desch, S. J., Ciesla, F. J., Hood, L. L., & Nakamoto, T. 2005, ASP Conf. Ser. 341: Chondrites and the Protoplanetary Disk, 341, 849

Dorschner, J., Begemann, B., Henning, T., Jaeger, C., & Mutschke, H. 1995, A&A, 300, 503

Draine, B. T. 2003, Ann. Rev. Astron. Astrophys., 41, 241

Drake, M. J., & Righter, K. 2002, Nature, 416, 39

Dullemond, C. P., van Zadelhoff, G. J., & Natta, A. 2002, A&A, 389, 464

Fabian, D., Henning, T., Jäger, C., Mutschke, H., Dorschner, J., & Wehrhan, O. 2001, A&A, 378, 228

Gail, H.-P. 1998, A&A, 332, 1099

Gail, H.-P. 2003, LNP Vol. 609: Astromineralogy, 609, 55

Gail, H.-P. 2004, A&A, 413, 571

Greaves, J. S., et al. 2005, ApJ, 619, L187

Grim, R. E. 1968, *Clay Mineralogy* (New York: McGraw-Hill)

Guan, Y., & Zolensky, M. E. 1997, Lunar and Planetary Institute Conference Abstracts, 28, 487

Haisch, K. E., Lada, E. A., & Lada, C. J. 2001, ApJ, 553, L153

Hallenbeck, S. L., Nuth, J. A., III, & Nelson, R. N. 2000, ApJ, 535, 247

Harker, D. E., & Desch, S. J. 2002, ApJ, 565, L109

Harper, D. A., Loewenstein, R. F., & Davidson, J. A. 1984, ApJ, 285, 808

Hartmann, L. 1998, *Accretion Processes in Star Formation* (Cambridge: Cambridge University Press)

Hartmann, L., Calvet, N., Gullbring, E., & D'Alessio, P. 1998, ApJ, 495, 385

Hashimoto, A., & Grossman, L. 1987, Geochim. Cosmochim. Atca, 51, 1685

Henning, T. 1983, Astrophys. & Space Sci., 97, 405

Hillenbrand, L. A., Strom, S. E., Calvet, N., Merrill, K. M., Gatley, I., Makidon, R. B., Meyer, M. R., & Skrutskie, M. F. 1998, AJ, 116, 1816

Holland, W. S., et al. 1998, Nature, 392, 788

Ichikawa, O., & Ikeda, Y. 1995, Antarctic Meteorite Research, 8, 63

Ichikawa, O., & Kojima, H. 1996, Meteoritics and Planetary Science, vol. 31, page A66, 31, 66

Ida, A., Nakamoto, T., & Susa, H. 2001, Icarus, 153, 430

"Infrared Space Observatory." May 19, 2006.
URL: http://www.iso.vilspa.esa.es/

Jäger, C., Mutschke, H., Begemann, B., Dorschner, J., & Henning, T. 1994, A&A, 292, 641

Jäger, C., Molster, F. J., Dorschner, J., Henning, T., Mutschke, H., & Waters, L. B. F. M. 1998, A&A, 339, 904

Jäger, C., Dorschner, J., Mutschke, H., Posch, T., & Henning, T. 2003, A&A, 408, 193

"The James Webb Space Telescope." May 19, 2006.
URL: http://www.jwst.nasa.gov/

Keller, L. P., & Buseck, P. R. 1990, Lunar and Planetary Institute Conference Abstracts, 21, 619

Keller, L. P., & Zolensky, M. E. 1991, LPI Contributions, 773, 87

Kemper, F., Vriend, W. J., & Tielens, A. G. G. M. 2004, ApJ, 609, 826

Kenyon, S. J. 2002, The Publications of the Astronomical Society of the Pacific, 114, 265

Kenyon, S. J., & Bromley, B. C. 2004, ApJ, 602, L133

Kerridge, J. F., McSween, H. Y., & Bunch, T. E. 1994, Meteoritics, 29, 481

Kessler, M. F. 1991, Advances in Space Research, 11, 271

Kessler, M. F. 2002, Advances in Space Research, 30, 1957

Krishna Swamy, K. S. 2005, *Dust in the universe. Similarities and differences* World Scientific Series in Astronomy and Astrophysics, Vol. 7. (Singapore: World Scientific Publishing)

Krot, A. N., Scott, E. R. D., & Zolensky, M. E. 1995, Meteoritics, 30, 748

Krot, A. N., et al. 2001, Meteoritics and Planetary Science, 36, 1189

Kurucz, R. L. 1993, Kurucz CD-ROM, Cambridge, MA: Smithsonian Astrophysical Observatory, —c1993, December 4, 1993,

Lagrange, A.-M., Backman, D. E., & Artymowicz, P. 2000, Protostars and Planets IV, 639

Lauretta, D. S., Hua, X., & Buseck, P. R. 2000, Geochim. Cosmochim. Atca, 64, 3263

Lynden-Bell, D., & Pringle, J. E. 1974, M.N.R.A.S., 168, 603

MacPherson, G. J., Grossman, L., Beckett, J. R., & Allen, J. M. 1982, Lunar and Planetary Science Conference, 12, 1079

MacPherson, G. J., Bar-Matthews, M., Tanaka, T., Olsen, E., & Grossman, L. 1983, Geochim. Cosmochim. Atca, 47, 823

McCaughrean, M. J., & O'dell, C. R. 1996, AJ, 111, 1977

Meeus, G., Waters, L. B. F. M., Bouwman, J., van den Ancker, M. E., Waelkens, C., & Malfait, K. 2001, A&A, 365, 476

Metchev, S. A., Eisner, J. A., Hillenbrand, L. A., & Wolf, S. 2005, ApJ, 622, 451

"Michelle." May 19, 2006.
URL: http://www.gemini.edu/sciops/instruments/michelle/MichIndex.html

Min, M., Hovenier, J. W., & de Koter, A. 2003, A&A, 404, 35

"MIRSI: A Mid-Infrared Spectrometer and Imager." May 20, 2006.
URL: http://cfa-www.harvard.edu/mirsi/mirsi_spec.html

Morbidelli, A., Chambers, J., Lunine, J. I., Petit, J. M., Robert, F., Valsecchi, G. B., & Cyr, K. E. 2000, Meteoritics and Planetary Science, 35, 1309

Nagashima, K., Krot, A. N., & Yurimoto, H. 2004, Nature, 428, 921

Nakamura, R. 1998, Earth, Planets, and Space, 50, 587

Nesse, W. D. 2000, *Introduction to Mineralogy* (New York: Oxford University Press)

Noguchi, T., Nakamura, T., & Nozaki, W. 2002, Earth and Planetary Science Letters, 202, 229

Nuth, J. A., Brearley, A. J., & Scott, E. R. D. 2005, ASP Conf. Ser. 341: Chondrites and the Protoplanetary Disk, 341, 675

Okamoto, Y. K., et al. 2004, Nature, 431, 660

Podosek, F. A., & Cassen, P. 1994, Meteoritics, 29, 6

Pollack, J. B., Hollenbach, D., Beckwith, S., Simonelli, D. P., Roush, T., & Fong, W. 1994, ApJ, 421, 615

Prinn, R. G., & Fegley, B. 1987, Annual Review of Earth and Planetary Sciences, 15, 171

Raymond, S. N., Quinn, T., & Lunine, J. I. 2004, Icarus, 168, 1

Reach, W. T., Morris, P., Boulanger, F., & Okumura, K. 2003, Icarus, 164, 384

Rubin, A. E. 1997, Meteoritics and Planetary Science, 32, 231

Rucinski, S. M. 1985, AJ, 90, 2321

Rybicki, G. B., & Lightman, A. P. 1979, *Radiative Processes in Astrophysics* (New York: Wiley-Interscience)

Sandford, S. A. 1996, Meteoritics and Planetary Science, 31, 449

Schirmeyer, S., Hoppe, P., Stephan, T., Bischoff, A., & Jessberger, E. K. 1997, Lunar and Planetary Institute Conference Abstracts, 28, 1253

Schütz, O., Meeus, G., & Sterzik, M. F. 2005, A&A, 431, 165

Schütz, O., Meeus, G., & Sterzik, M. F. 2005, A&A, 431, 175

Scott, E. R. D., & Krot, A. N. 2005, ApJ, 623, 571

Shu, F. H., Adams, F. C., & Lizano, S. 1987, Ann. Rev. Astron. Astrophys., 25, 23

Simon, S. B., & Grossman, L. 2003, Meteoritics and Planetary Science, 38, 813

Sitko, M. L., Sprague, A. L., & Lynch, D. K. 2000, ASP Conf. Ser. 196: Thermal Emission Spectroscopy and Analysis of Dust, Disks, and Regoliths, 196,

"SOFIA." May 19, 2006. URL: http://www.sofia.usra.edu/

Spangler, C., Sargent, A. I., Silverstone, M. D., Becklin, E. E., & Zuckerman, B. 2001, ApJ, 555, 932

Spitzer Space Telescope Observer's Manual - Version 5.0 2004

Steele, I. M. 1995, Meteoritics, 30, 9

Su, K. Y. L., et al. 2005, ApJ, 628, 487

"T-ReCS." May 19, 2006.
URL: http://www.gemini.edu/sciops/instruments/miri/MiriIndex.html

"TEXES." May 19, 2006.
URL: http://www.gemini.edu/sciops/instruments/texes/TexesIndex.html

Tomeoka, K., & Buseck, P. R. 1985, Geochim. Cosmochim. Atca, 49, 2149

Tomeoka, K., & Buseck, P. R. 1990, Geochim. Cosmochim. Atca, 54, 1745

Tomeoka, K. 1993, Meteoritics, 28, 450

van Boekel, R., et al. 2004, Nature, 432, 479

van de Hulst, H. C. 1957, *Light Scattering by Small Particles* (New York: John Wiley)

Velde, B. (Ed.) 1995, *Origin and Mineralogy of Clays. Clays and the Environment* (Berlin: Springer)

Wadhwa, M., & Russell, S. S. 2000, Protostars and Planets IV, 995

Waelkens, C., et al. 1996, A&A, 315, L245

Wahhaj, Z., Koerner, D. W., Ressler, M. E., Werner, M. W., Backman, D. E., & Sargent, A. I. 2003, ApJ, 584, L27

Weaver, C. E. 1989, *Clays, Muds, and Shales (Developments in Sedimentology 44)* (New York: Elsevier Science Publishing Company)

Wehrstedt, M., & Gail, H.-P. 2003, A&A, 410, 917

Weidenschilling, S. J. 1977, Astrophys. & Space Sci., 51, 153

Weisberg, M. K., Prinz, M., Boesenberg, J. S., Kozhushko, G., Clayton, R. N., Mayeda, T. K., & Ebihara, M. E. 1996, Lunar and Planetary Institute Conference Abstracts, 27, 1407

Weisberg, M. K., & Prinz, M. 1998, Meteoritics and Planetary Science, 33, 1087

Woolum, D. S., & Cassen, P. 1999, Meteoritics and Planetary Science, 34, 897

Zolensky, M. E., Weisberg, M. K., Buchanan, P. C., Prinz, M., Reid, A., & Barrett, R. A. 1992, Lunar and Planetary Institute Conference Abstracts, 23, 1587

Zolensky, M. E., Hyman, M., Rowe, M. W., & Weisberg, M. K. 1996, Lunar and Planetary Institute Conference Abstracts, 27, 1505